catalysts

MDPI

Article

# Kinetic and Mechanistic Study of Rhodamine B Degradation by $H_2O_2$ and $Cu/Al_2O_3/g\text{-}C_3N_4$ Composite

**Chunsun Zhou †, Zhongda Liu †, Lijuan Fang, Yulian Guo, Yanpeng Feng and Miao Yang ***

School of Chemistry, Chemical Engineering and Life Sciences, Wuhan University of Technology, 122 Luoshi Road, Wuhan 430070, China; zhouchunsun@whut.edu.cn (C.Z.); liuzhongda@whut.edu.cn (Z.L.); fanglijuan@whut.edu.cn (L.F.); guoyulian@whut.edu.cn (Y.G.); fengyanpeng1996@gmail.com (Y.F.)

* Correspondence: yangmiao@whut.edu.cn; Tel.: +86-1898-617-6465

† Authors contributed equally to this work and are recognized as co-first authors.

Received: 25 January 2020; Accepted: 9 March 2020; Published: 10 March 2020

**Abstract:** The classic Fenton reaction, which is driven by iron species, has been widely explored for pollutant degradation, but is strictly limited to acidic conditions. In this work, a copper-based Fenton-like catalyst $Cu/Al_2O_3/g\text{-}C_3N_4$ was proposed that achieves high degradation efficiencies for Rhodamine B (Rh B) in a wide range of pH 4.9–11.0. The $Cu/Al_2O_3$ composite was first prepared via a hydrothermal method followed by a calcination process. The obtained $Cu/Al_2O_3$ composite was subsequently stabilized on graphitic carbon nitride ($g\text{-}C_3N_4$) by the formation of C−O−Cu bonds. The obtained composites were characterized through FT-IR, XRD, TEM, XPS, and $N_2$ adsorption/desorption isotherms, and the immobilized $Cu^+$ was proven to be active sites. The effects of Cu content, $g\text{-}C_3N_4$ content, $H_2O_2$ concentration, and pH on Rh B degradation were systematically investigated. The effect of the catalyst dose was confirmed with a specific reaction rate constant of $(5.9 \pm 0.07) \times 10^{-9}$ m·s$^{-1}$ and the activation energy was calculated to be 71.0 kJ/mol. In 100 min 96.4% of Rh B (initial concentration 20 mg/L, unadjusted pH (4.9)) was removed in the presence of 1 g/L of catalyst and 10 mM of $H_2O_2$ at 25 °C, with an observed reaction rate constant of $6.47 \times 10^{-4}$ s$^{-1}$. High degradation rates are achieved at neutral and alkaline conditions and a low copper leaching (0.55 mg/L) was observed even after four reaction cycles. Hydroxyl radical (HO·) was identified as the reactive oxygen species by using isopropanol as a radical scavenger and by ESR analysis. HPLC-MS revealed that the degradation of Rh B on $Cu/Al_2O_3/CN$ composite involves N-de-ethylation, hydroxylation, de-carboxylation, chromophore cleavage, ring opening, and the mineralization process. Based on the results above, a tentative mechanism for the catalytic performance of the $Cu/Al_2O_3/g\text{-}C_3N_4$ composite was proposed. In summary, the characteristics of high degradation rate constants, low ion leaching, and the excellent applicability in neutral and alkaline conditions prove the $Cu/Al_2O_3/g\text{-}C_3N_4$ composite to be a superior Fenton-like catalyst compared to many conventional ones.

**Keywords:** $Cu/Al_2O_3/g\text{-}C_3N_4$; Fenton-like; $H_2O_2$; hydroxyl radical; Rhodamine B

## 1. Introduction

With the rapid development of industry, persistent organic pollutants in water have attracted widespread attention due to their persistence, bioaccumulation, and high toxicity [1,2]. So far, advanced oxidation processes (AOPs) have been found to be one of the most promising methods to treat persistent organic pollutants in water [3–7]. Due to the in-situ formed highly reactive and non-selective hydroxyl radicals (HO·) during the process, AOPs are capable of mineralizing almost all organic compounds to $CO_2$, $H_2O$, and small organic compounds [8–11].

As a typical AOP, Fenton reaction is efficient for HO· production, but still faces some limitations, such as the strict acidic pH range (pH < 4) [12,13], formation of iron sludge [14,15], and high cost for catalyst recycling [16,17]. A number of non-ferrous metals, such as copper [18], manganese [19], and titanium [20], have been developed as alternatives. In particular, $Cu^+$ reacts with $H_2O_2$ in a similar manner to $Fe^{2+}$, but with a much higher reaction rate constant (as shown in Equations (1) and (2)). In contrast to $Fe^{3+}$ that forms the insoluble $[Fe(H_2O)_6]^{3+}$ complex at pH > 5, $Cu^{2+}$ forms the aquo complex $[Cu(H_2O)_6]^{2+}$ that predominates at neutral conditions, making $Cu^+$ own a wider pH range for application [21]. Additionally, it is known that $Cu^{2+}$ could form certain complexes with organic degradation intermediates, which could react with $H_2O_2$ to generate more HO· [22].

$$Fe^{2+} + H_2O_2 \rightarrow Fe^{3+} + HO\cdot + OH^- \qquad (k = 63 - 76\ M^{-1}\cdot s^{-1}) \tag{1}$$

$$Cu^+ + H_2O_2 \rightarrow Cu^{2+} + HO\cdot + OH^- \qquad (k = 1.0 \times 10^4\ M^{-1}\cdot s^{-1}) \tag{2}$$

However, $Cu^+$ ions are prone to disproportionation in acidic aqueous solution and can be easily oxidized by dissolved $O_2$, thereby limiting the application in the aqueous environment [23]. One common strategy for the preparation of copper-based catalysts is the immobilization of copper species on support materials, for example, the immobilization of $Cu^+/Cu^{2+}$, copper oxide, or the copper-organic complex [24] on various matrixes like metal oxides [25–27], molecular sieve [28,29], and graphitic carbon nitride (g-$C_3N_4$) [30,31].

With a suitable band gap (2.7 eV) and high response to visible light, g-$C_3N_4$ has been intensively explored as a photocatalyst for energy and environmental applications [3,32–34]. Apart from this, g-$C_3N_4$ could also be applied as a Fenton-like catalyst in the absence of light irradiation through the combination with other materials [35,36]. g-$C_3N_4$ has a 2D planar structure in which tri-s-triazine units are connected by tertiary amines. Typical π-conjugated graphitic planes are formed via the $sp^2$ hybridization of carbon and nitrogen atoms [37], which brings a large specific surface area, thus providing more reaction sites for heterogeneous reaction. Besides, g-$C_3N_4$ shows strong affinity for $H_2O_2$ and could easily adsorb them to the surface, thereby providing larger chances for their contact with other catalytic materials loaded on g-$C_3N_4$ [34]. Additionally, numerous external groups (−$NH_2$, −NH, −N, and −OH) on the surface may serve as strong Lewis base sites for nanoparticle deposition or metal inclusion [38]. The incorporation of metallic elements into the g-$C_3N_4$ matrix could induce the production of delocalized electrons, which promotes the catalytic reactions [36,39]. As a typical example, Xu et al. constructed the Cu-$Al_2O_3$-g-$C_3N_4$ system, in which a small amount of g-$C_3N_4$ was used to coordinate with Cu ions to induce the formation of an electron-rich Cu centre and decrease the electron density of the π-electron conjugated system through cation-π interactions [40].

Inspired by the above-mentioned research, a similar but distinguishing efficient Cu/$Al_2O_3$/g-$C_3N_4$ composite was proposed in this work, with which $H_2O_2$ activating was promoted in a different approach. Copper species were bonded to the $Al_2O_3$ framework to act as the catalytic component and g-$C_3N_4$ was used in large amounts to act as support for the Cu/$Al_2O_3$ composite. The decomposition of $H_2O_2$ was promoted by the strong adsorption of $H_2O_2$ on the g-$C_3N_4$ matrix. The obtained composites were characterized through Fourier transform infrared (FT-IR) spectroscopy, X-ray diffraction (XRD), transmission electron microscopy (TEM), X-ray photoelectron spectroscopy (XPS), and $N_2$ adsorption/desorption isotherms. The optimal synthetic parameters and experimental conditions, including the Cu content, g-$C_3N_4$ content, $H_2O_2$ concentration, and pH value were determined. Besides, the effect of the catalyst dose and temperature were confirmed by calculating specific reaction rate constant and activation energy, and the durability and low leaching were evaluated in recycling experiment. In addition, the reactive oxygen species generated in the present system were identified by scavenging experiments and electron spin resonance (ESR) analysis, while the degradation products of Rh B were identified by high performance liquid chromatography-mass spectrometry (HPLC-MS)

analysis. Based on the results, the catalytic mechanism of Rh B degradation on $Cu/Al_2O_3/g\text{-}C_3N_4$ composite was proposed.

## 2. Results and Discussion

### *2.1. Structural Characterization of Composites*

$Cu_{12}/Al_2O_3$ and $Cu_{12}/Al_2O_3/CN_{1.3}$ (the naming rules of catalysts are indicated in experimental section) were selected as the typical $Cu/Al_2O_3$ and $Cu/Al_2O_3/CN$ composite to compare their structures with $Al_2O_3$ and CN. The FT-IR spectra of $Al_2O_3$, $Cu/Al_2O_3$, CN, and $Cu/Al_2O_3/CN$ samples were recorded to distinguish the functional groups. As shown in Figure 1, the two peaks at 1513 $cm^{-1}$ and 1636 $cm^{-1}$ in the FT-IR spectra of $Al_2O_3$ and $Cu/Al_2O_3$ are attributed to the C=C vibrations and C=O vibrations, which are derived from glucose added in the preparation process [40]. As observed for CN, the sharp peak at 810 $cm^{-1}$ is ascribed to the breathing mode of tri-s-triazine units, and the peaks in the region of 1200−1600 $cm^{-1}$ are assigned to the stretching vibration of the CN heterocycle [31]. In addition, the peak at 3173 $cm^{-1}$ corresponds to the N−H stretching vibration [36]. All these characteristic peaks could be observed in the $Cu/Al_2O_3/CN$ composite, indicating that the chemical structure of CN was not affected by the introduction of $Cu/Al_2O_3$.

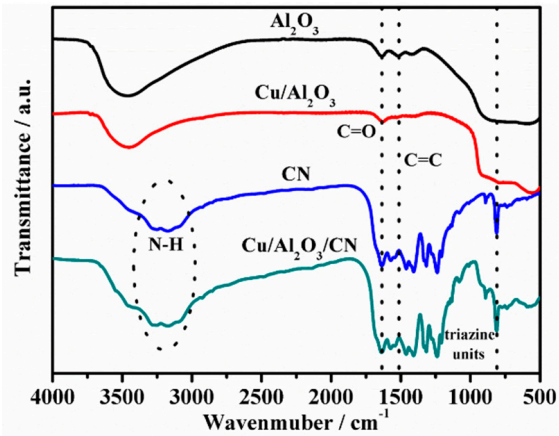


**Figure 1.** FT-IR spectra of $Al_2O_3$, $Cu/Al_2O_3$, CN, and $Cu/Al_2O_3/CN$ samples.

The X-ray diffraction patterns of $Al_2O_3$, $Cu/Al_2O_3$, CN, and $Cu/Al_2O_3/CN$ samples were investigated to determine the crystalline structures, as presented in Figure 2. It is clearly observed that the major crystalline structure of $Al_2O_3$ is the γ-alumina phase (JCPDS No. 10-0425) [41]. In comparison with pure $Al_2O_3$, new peaks are founded at 35.2°, 38.5°, 48.8°, 53.4°, 58.2°, 66.2°, and 68.1° in the XRD pattern of $Cu/Al_2O_3$, which represent the (002), (111), (20-2), (020), (202), (31-1), and (220) planes of the copper oxide phase (JCPDS No. 48-1548), respectively [40]. The peak at 61.5° is referred to the diffraction of the (220) plane of cuprous oxide phase (JCPDS No. 65-3288) [42]. These results imply that the copper species were successfully bonded to the $Al_2O_3$ framework. From the pattern of CN, two main diffraction peaks could be found at 13.0° and 26.9°, which correspond to the interlayer stacking (100) plane of tri-s-triazine units and the (002) plane arising from the interlayer stacking of aromatic systems (JCPDS No. 87-1526) [43]. All the diffraction peaks of $Cu/Al_2O_3$ and CN could be found in the pattern of $Cu/Al_2O_3/CN$ composite, indicating the successful synthesis of the $Cu/Al_2O_3/CN$ composite.

The microstructures of $Al_2O_3$, $Cu/Al_2O_3$, CN, and $Cu/Al_2O_3/CN$ samples were analyzed by TEM. The results are shown in Figure 3. As can be seen in Figure 3A,B, the lattice spacing was confirmed to be 0.29 nm, which corresponds to the (220) lattice planes of γ-alumina [44], and was consistent with the results obtained by XRD. In Figure 3C, it can be seen that the copper bonded alumina framework was rod like. The lattice spacing in Figure 3D was confirmed to be 0.24 nm, which corresponds to the (111) lattice planes of copper oxide confirmed by XRD [45]. In Figure 3E, it is clear that CN shows

a two-dimensional structure with a wide pore size distribution [35]. According to Figure 3F, it can be observed that the rod like $Cu/Al_2O_3$ was embedded in the CN matrix, indicating the successful combination of $Cu/Al_2O_3$ and CN.

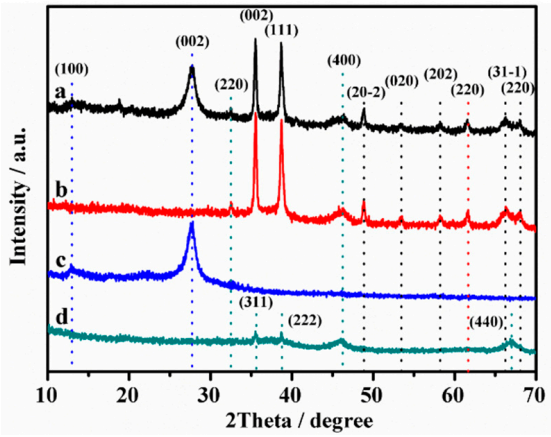


**Figure 2.** XRD patterns of the synthesized samples (**a**) $Cu/Al_2O_3/CN$, (**b**) $Cu/Al_2O_3$, (**c**) CN, and (**d**) $Al_2O_3$.

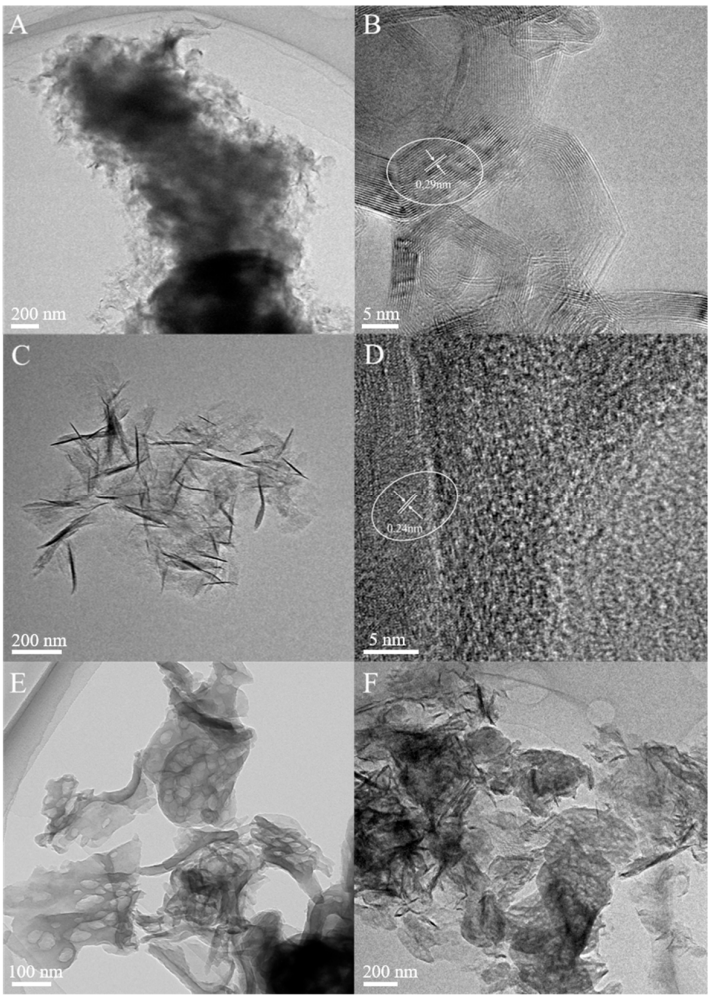


**Figure 3.** TEM images of (**A**,**B**) $Al_2O_3$, (**C**,**D**) $Cu/Al_2O_3$, (**E**) CN, and (**F**) $Cu/Al_2O_3/CN$.

The XPS spectra of the $Cu/Al_2O_3/CN$ composite before and after the reaction were obtained to investigate its surface chemical states and elemental composition. The results are shown in Figure 4

and Table 1. The peaks of the C 1s spectrum at 281.5 eV and 284.6 eV were assigned to C−H and C−C, respectively. Notably, the peak at 285.1 eV was attributed to C−O−H or C−O−metal, which could confirm that $Cu/Al_2O_3$ was stabilized on the CN matrix by the C−O−Cu bonds [36,40]. For N 1s, the peaks at 395.1 eV, 395.7 eV, and 397.1 eV were ascribed to triazine rings C−N−C, tertiary nitrogen $N-(C)_3$, and $sp^2$-type C=N bond, indicating that the structure of CN was not changed [36]. The XPS spectrum of Cu 2p in Figure 4C displayed three main peaks at 932.0 eV, 934.0 eV, and 941.5 eV, which correspond to $Cu^+$, $Cu^{2+}$, and satellite peaks of copper species, respectively [40,41]. As the binding energy of $Cu^+$ and $Cu^0$ are very close, it is difficult to distinguish between $Cu^+$ and $Cu^0$ by the XPS feature of Cu $2p_{3/2}$. The Cu LMM peak is normally applied to distinguish between the $Cu^0$ and $Cu^+$ according to previous studies [46,47]. However, due to the relatively low copper content in the sample, the presence of $Cu^+$ cannot be judged by the Cu LMM peak. The results of the XRD patterns could be used instead to confirm the presence of $Cu^+$. Two peaks of the Al 2p spectrum were observed at 74.1 eV and 75.0 eV in Figure 4D, which were attributed to Al−O−Al and Al−O−Cu, indicating that copper species were bonded to $Al_2O_3$ framework [46]. The Cu 2p XPS spectrum of the used $Cu/Al_2O_3/CN$ composite is shown in Figure 4E. The peaks at 931.7 eV, 933.6 eV, and 941.5 eV still represent $Cu^+$, $Cu^{2+}$, and satellite peaks of copper species, respectively. The $Cu^+$ to $Cu^{2+}$ ratio on the $Cu/Al_2O_3/CN$ composite was 2.34 before reaction and decreased to 1.42 after reaction, indicating that copper species were the active sites and the conversion of $Cu^+$ to $Cu^{2+}$ was involved in the reaction [48].

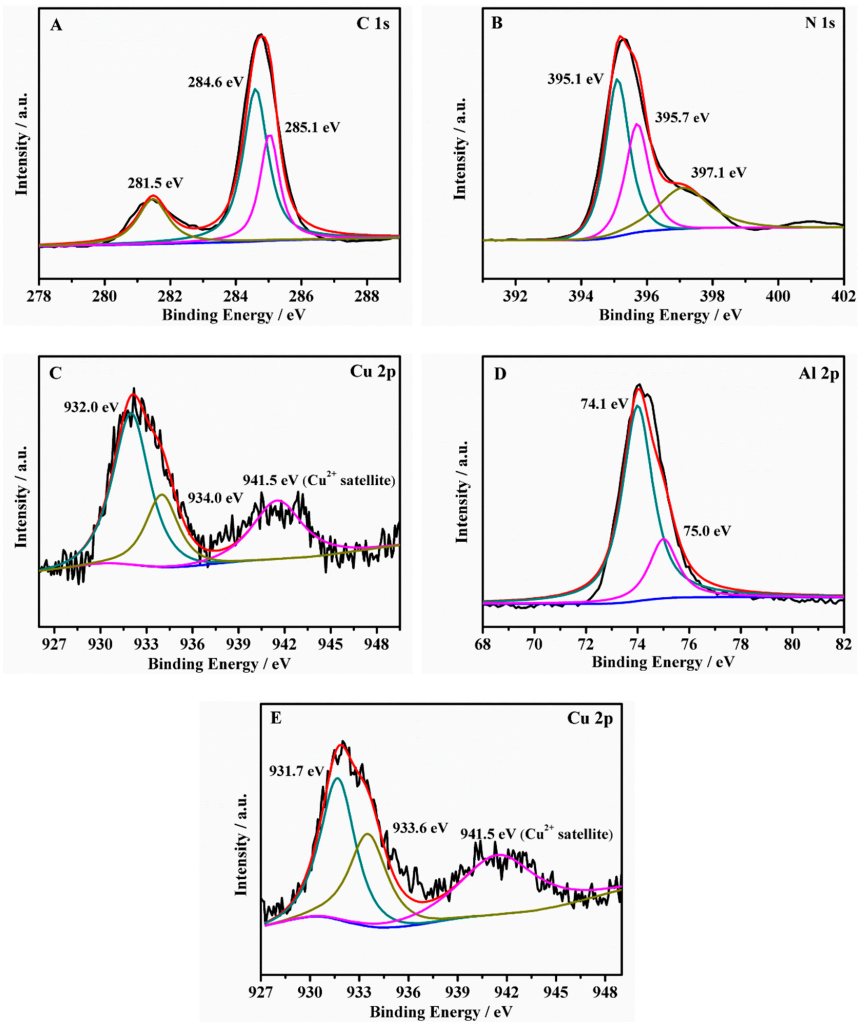


**Figure 4.** (**A**) C 1s, (**B**) N 1s, (**C**) Cu 2p, and (**D**) Al 2p XPS spectra of $Cu/Al_2O_3/CN$ composite before reaction, and (**E**) Cu 2p spectrum of the $Cu/Al_2O_3/CN$ composite after reaction.

**Table 1.** XPS results of the $Cu/Al_2O_3/CN$ composite.

| | BE/eV | Chemical Bonds | | BE/eV | Chemical Bonds |
|---|---|---|---|---|---|
| C 1s | 281.5 | C−H | N 1s | 395.1 | C−N−C |
| | 284.6 | C−C | | 395.7 | $N-(C)_3$ |
| | 285.1 | C−O | | 397.1 | C=N |
| Cu 2p | 932.0/931.7 | $Cu^+$ | Al 2p | 74.1 | Al−O−Al |
| | 934.0/933.6 | $Cu^{2+}$ | | 75.0 | Al−O−Cu |

BE denotes the binding energy.

The $N_2$ adsorption/desorption isotherm and the pore size distribution of the $Al_2O_3$, $Cu/Al_2O_3$, CN, and $Cu/Al_2O_3/CN$ samples are shown in Figure 5. The specific surface area of $Al_2O_3$ reaches 133.1 ± 0.5 $m^2/g$ with a pore width of 6.7 nm, and the introduction of copper species leads to a decline to 119.5 ± 1.0 $m^2/g$ and 5.3 nm, respectively. All the CN containing samples show typical IV isotherms with the H3 hysteresis loop, indicating the existence of a typical mesoporous structure with slit-like pores in CN [22]. Additionally, when $Cu/Al_2O_3$ was stabilized on the CN matrix, the specific surface area increased from 72.2 ± 0.9 $m^2/g$ for CN to 146.6 ± 1.0 $m^2/g$ for $Cu/Al_2O_3/CN$, which is more beneficial for the adsorption of organic pollutants and $H_2O_2$ on the catalyst surface and proves that the fabrication of the $Cu/Al_2O_3/CN$ composite is not merely a physical mixing process. In summary, a higher specific surface area and smaller pore width are achieved in the $Cu/Al_2O_3/CN$ composite.

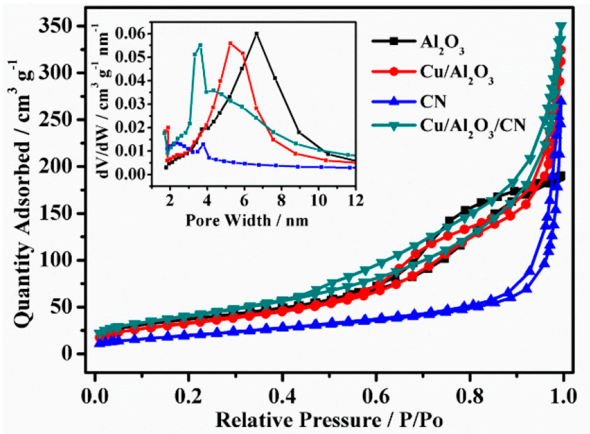


**Figure 5.** $N_2$ adsorption/desorption isotherm and the pore size distribution (insert) of the $Al_2O_3$, $Cu/Al_2O_3$, CN, and $Cu/Al_2O_3/CN$.

## 2.2. Catalytic Performance of Composites

The effect of Cu content, CN content, $H_2O_2$ concentration, and pH value were investigated to obtain the optimal synthetic parameters and reaction conditions. Besides, the effect of the catalyst dose and temperature was confirmed by calculating the specific reaction rate constant and activation energy ($E_a$). The durability and ion leaching of the composite were evaluated by the recycling experiments. In addition, the reactive species generated were identified by ESR analysis and radical scavenging experiments, and then the catalytic mechanism of Rh B on $Cu/Al_2O_3/CN$ composite was proposed by confirming intermediates using HPLC-MS.

### 2.2.1. Effect of Cu Content

In order to obtain the optimal Cu content for catalyst fabrication, a series of $Cu_x/Al_2O_3$ composites (x = 0, 4, 7, 9, 12, and 15 wt %) were prepared to compare their catalytic performances on the removal of Rh B in the presence of $H_2O_2$. As shown in Figure 6, in the absence of copper decoration, $Al_2O_3$ exhibited negligible catalytic capacity for Rh B degradation, with 3.0% Rh B removed in 100 min. The degradation was enhanced by copper doping and the rate progressively increased from x = 0 to

x = 12, after which the degradation rate started to decrease. During the synthesis process of $Cu/Al_2O_3$ composite, copper species were bonded to the $Al_2O_3$ framework. However, there is an upper limit (x = 12) for the amount of copper species that could enter the $Al_2O_3$ framework, so part of the copper species would be present as the extra framework if excess copper was introduced [47]. The extra framework copper species may impede the contact between $H_2O_2$ and framework copper species, thereby limiting the decomposition of $H_2O_2$ [22,41]. Therefore, the optimal Cu content was confirmed to be x = 12 and $Cu_{12}/Al_2O_3$ was selected as optimal components for further studies.

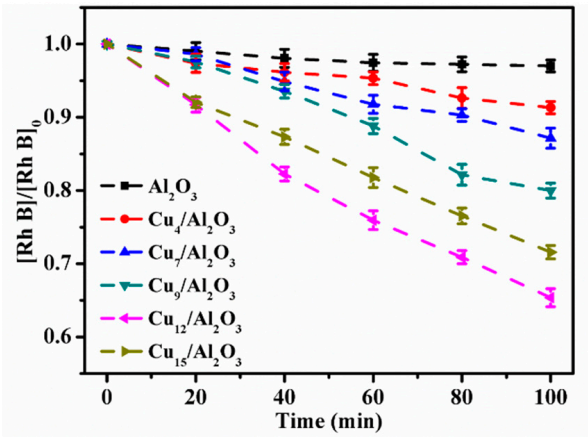


**Figure 6.** [Rh B]/[Rh B]$_0$ as a function of time in the presence of 1 g/L $Cu_x/Al_2O_3$ composite (x = 0, 4, 7, 9, 12, and 15 wt %). Reaction conditions: [Rh B]$_0$ = 20 mg/L, [$H_2O_2$]$_0$ = 10 mM, V = 100 mL, T = 25 °C, pH 4.9 (unadjusted).

### 2.2.2. Effect of CN Content

A fixed amount (0.1 g) of the $Cu_{12}/Al_2O_3$ composite was loaded on different amounts of CN to determine the optimal CN content. The degradation of Rh B in the presence of $Cu_{12}/Al_2O_3/CN_y$ (y = 0, 0.7, 1.3, 2.0, and 2.7 wt %) is presented in Figure 7. As shown, the $Cu_{12}/Al_2O_3$ composite shows acceptable catalytic property for Rh B degradation, removing 34.6% Rh B in 100 min. Additionally, it is apparent that the introduction of CN leads to a corresponding enhancement of the degradation rate. With CN incorporated, part of $Al_2O_3/Cu_{0.9}$ was stabilized on CN sheets by the formation of C−O−Cu bonds. Aqueous $H_2O_2$ are easily bonded to the surface of CN [34], providing larger chances for its contact with immobilized $Cu^+$, which brought a significant improvement in catalytic property. Consequently, the degradation ratio within 100 min increased from 34.6% to 96.4% in the CN range of y = 0 to y = 1.3. However, excess CN incorporation from y = 1.3 to y = 2.7 did not further improve the degradation ratio. In the presence of adequate CN (y = 1.3), $Cu_{12}/Al_2O_3$ is fully loaded on the CN interlayers, resulting in the largest degradation ratio exhibited in Figure 7. When the amount of CN was largely in excess to $Cu_{12}/Al_2O_3$, the mass ratio of $Cu_{12}/Al_2O_3$ in $Cu/Al_2O_3/CN$ decreased accordingly, thereby limiting the further improvement of catalytic property. Therefore, the optimal CN content was confirmed as y = 1.3 and $Cu_{12}/Al_2O_3/CN_{1.3}$ was selected as the typical composite for further studies. The $Cu/Al_2O_3/CN$ composite in the following text refers to the $Cu_{12}/Al_2O_3/CN_{1.3}$ composite unless addition descriptions were used.

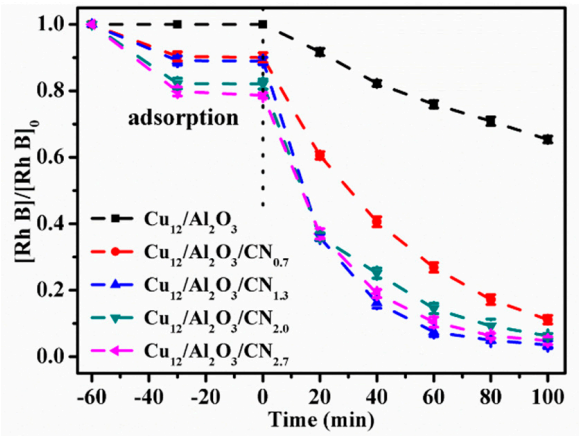


**Figure 7.** [Rh B]/[Rh B]$_0$ as a function of time in the presence of 1 g/L $Cu_{12}/Al_2O_3/CN_y$ composite (y = 0, 0.7, 1.3, 2.0, and 2.7 wt %). Reaction conditions: [Rh B]$_0$ = 20 mg/L, [$H_2O_2$]$_0$ = 10 mM, V = 100 mL, T = 25 °C, pH 4.9 (unadjusted).

### 2.2.3. Synergistic Effect

To verify the synergistic effect of $Cu_{12}/Al_2O_3$ and CN on the degradation of Rh B, four samples were prepared and their catalytic properties were compared in the same condition. The results are presented in Figure 8. It can be seen that both $Cu_{12}/Al_2O_3$ and CN show a weak catalytic property. Notably, CN exhibited a fine adsorption capacity for Rh B, which is attributed to its large specific surface area and multiple groups on the surface. By physically mixing $Cu_{12}/Al_2O_3$ and CN, the adsorption capacity for Rh B decreased but a higher degradation rate was observed. This may be attributed to the fact that immobilized copper species form an adsorption competition with Rh B on CN sheets, leading to a portion of adsorptive sites occupied by immobilized copper, which lowers the adsorption of Rh B but accelerates its degradation. In the $Cu/Al_2O_3/CN$ composite, much stronger bonds were formed between Cu and C−O−H as C−O−Cu, leading to a much lower adsorption capacity and a synergistically enhanced degradation property for Rh B.

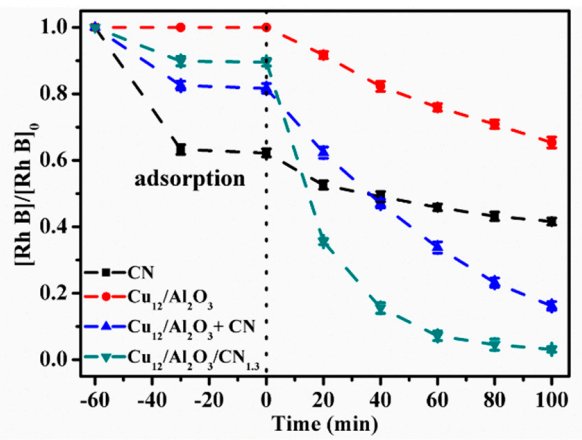


**Figure 8.** [Rh B]/[Rh B]$_0$ as a function of time in the presence of 1 g/L different samples. Reaction conditions: [Rh B]$_0$ = 20 mg/L, [$H_2O_2$]$_0$ = 10 mM, V = 100 mL, T = 25 °C, pH 4.9 (unadjusted).

### 2.2.4. Effect of pH

The homogeneous Fenton reaction is strictly limited to acidic conditions (pH < 4), which limits its application in neutral and alkaline conditions [4,12]. Therefore, the effect of pH is an important criterion for the evaluation of catalytic performance of catalysts, especially the ones that involve potential dissolved metal ion species. To evaluate the practical applicability of the $Cu/Al_2O_3/CN$

composite in various pH conditions, a series of experiments were carried out ranging from pH 3.0 to pH 11.0. The initial pH value of 20 mg/L Rh B is 4.9, so this value (unadjusted pH) was used as a replacement of pH 5.0. The Rh B solutions were adjusted to predetermined pH values with the addition of 1 M HCl or NaOH. In all the experiments, the initial pH values underwent a slight increase with the extent of 1.0 ± 0.3 units, which could be attributed to the formation of $OH^-$ in the $H_2O_2$ decomposition process. The degradation of Rh B is shown in Figure 9. It is evident that rapid degradations of Rh B were achieved at pH values higher than pKa of Rh B (3.7), and a lower pH value of 3.0 led to a remarkable repression. This is mainly attributed to the different existence forms of Rh B at different pH conditions. At pH values higher than 3.7, the carboxyl group of cationic $RhB^+$ is deprotonated and the dye is transformed into zwitterionic $RhB^{\pm}$ with a higher hydrophilic character that is prone to reacting with HO· radical [49]. Additionally, the scavenging effect of HO· radical by $H^+$ becomes stronger at low pH values [50,51], and $H_2O_2$ would become more stable under strong acid conditions to form oxonium $[H_3O_2]^+$, which inhibits its reaction with active species to generate HO· radical in the presence of a large amount of $H^+$ [48]. According to the Eh-pH diagram of Cu-$H_2O$ [52,53], CuO and $Cu_2O$ remain stable under alkaline conditions, which is beneficial for the catalytic degradation of Rh B. Despite the fact that more $O_2{\cdot}^-$ radicals are produced in alkaline conditions that consumes HO· radical and $H_2O_2$, the degradation rates did not decline in higher pH conditions and even remarkably increased at pH 11.0, which may be attributed to the change of hydrophobic property of the dye and its interaction with negatively charged catalyst surface in strong alkaline conditions [49]. In summary, a remarkable degradation rate could be achieved in neutral and alkaline conditions, which is superior to classic Fenton reaction. Since there is no drastic difference in the removal of Rh B in the range of pH 4.9–9.0, Rh B solution with the unadjusted pH value of 4.9 was used for subsequent experiments.

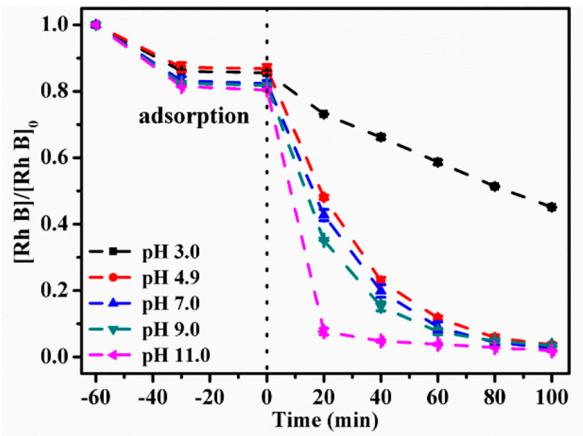


**Figure 9.** [Rh B]/[Rh B]$_0$ as a function of time with the different pH conditions in the presence of 1 g/L of the Cu/$Al_2O_3$/CN composite. Reaction conditions: [Rh B]$_0$ = 20 mg/L, [$H_2O_2$]$_0$ = 10 mM, V = 100 mL, T = 25 °C.

### 2.2.5. Effect of $H_2O_2$ Concentration

Since $H_2O_2$ is the main source of HO· in the Fenton-like reaction, the effect of $H_2O_2$ on the degradation of Rh B in the presence of Cu/$Al_2O_3$/CN composite was investigated. As calculated by Equation (3), the stoichiometric amount of $H_2O_2$ to achieve total mineralization of 20 mg/L Rh B was calculated to be 3.0 mM, and the effect of $H_2O_2$ concentration was investigated in the range of 1–10 mM.

$$C_{28}H_{31}ClN_2O_3 + 73\ H_2O_2 \rightarrow 28\ CO_2 + 87\ H_2O + HCl + 2\ HNO_3 \quad (3)$$

The evolution of $H_2O_2$ with an initial concentration of 10 mM was taken as an example for kinetics analysis, the result of which is presented in Figure S1A. The residual concentration of $H_2O_2$ evolves linearly with reaction time, demonstrating the zero-order reaction kinetics during the reaction, which

is attributed to the fact that $H_2O_2$ was present in large excess compared to Rh B. Only 11.9% of $H_2O_2$ was consumed in this experiment, which is far less significant than the Rh B decline that reached up to 96.4%. Therefore, more emphasis was stressed on the evolution of Rh B in this work. The normalized concentration of Rh B ([Rh B]/[Rh B]$_0$) and its logarithm are plotted as a function of the reaction time in Figure S1B,C for kinetic analysis. The plot of ln([Rh B]/[Rh B]$_0$) versus reaction time was linearly fitted with an $R^2$ of 0.9913, which demonstrated that the Rh B decline followed a pseudo first-order kinetics, as confirmed by some photocatalytic and Fenton-like systems [48,54]. The negative slope of the fitted curve represents the observed reaction rate constant $k_{obs}$, which was $5.14 \times 10^{-4}$ $s^{-1}$ for this experiment. The decline of Rh B with different initial $H_2O_2$ concentrations was recorded in Figure 10 together with the corresponding reaction rate constants. As expected, the degradation rate increased with increasing $H_2O_2$ concentration. The initial $H_2O_2$ concentration of 10 mM led to an efficient degradation with a rate constant of $5.14 \times 10^{-4}$ $s^{-1}$, which is a satisfactory value for subsequent activity evaluations. Certainly, larger reaction rates could be achieved with higher $H_2O_2$ concentrations, but considering the fact that $H_2O_2$ also acts as an HO· scavenger (as shown in Equation (4)) that lowers the efficiency of using $H_2O_2$, exorbitant concentrations were not used [4]. The emphasis is not to seek for an 'optimal' $H_2O_2$ concentration, so $[H_2O_2]_0$ was fixed at 10 mM for other experiments in this work.

$$H_2O_2 + HO\cdot \rightarrow HO_2\cdot + H_2O \quad (4)$$

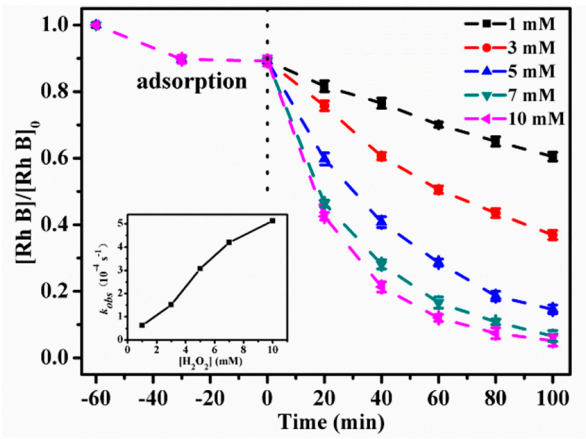


**Figure 10.** [Rh B]/[Rh B]$_0$ as a function of time and the corresponding reaction rate constants (insert) with different $H_2O_2$ concentrations in the presence of 1 g/L of the Cu/$Al_2O_3$/CN composite at room temperature. Reaction conditions: [Rh B]$_0$ = 20 mg/L, V = 100 mL, pH 4.9 (unadjusted).

### 2.2.6. The Effect of the Catalyst Dose

The value of $k_{obs}$ describes the rate that a reaction happens, and this value is dependent on the dose of the catalyst, which means a larger amount of the catalyst leads to a larger reaction rate constant. In this work, different amounts of catalyst (0.4–1.0 g/L) were used to catalyze Rh B degradation to check the effect of the catalyst dose on the reaction rate. Considering the facts that surface reaction dominates in heterogeneous systems and surface area plays a significant role, it would be unfair to use mass concentration for intersystem comparisons, which does not give consideration to the particle size and shape. Thus, in this work, the catalyst dose is represented by surface area concentration (SA/V), which is the product of mass concentration (g/L) and specific surface area ($m^2$/g) and has a unit of $m^{-1}$. The concept of surface area concentration was first proposed by Matheson and Tratnyek as a general independent variable to correlate with the contaminants removal rate constants, as it incorporates most of the effects of grain size and shape [55], and now it is widely used in many heterogeneous systems

for kinetic study [35,56–59]. One example for the unit conversion is exhibited in Equation (5), with a mass concentration of 1 g/L and the specific surface area of 146.6 $m^2/g$ for the $Cu/Al_2O_3/CN$ composite.

$$\frac{SA}{V} = 1\,g/L \times 146.6\,m^2/g = 146.6\,m^2/L = 146.6\,m^2/(10^{-3}\,m^3) = 1.466\times10^5\,m^2/m^3 = 1.466\times10^5\,m^{-1} \quad (5)$$

Figure 11A depicts ln([Rh B]/[Rh B]$_0$) as a function of time with different surface area concentrations (SA/V) of catalyst at 25 °C. All the ln([Rh B]/[Rh B]$_0$) plots were linearly fitted with reaction time, reconfirming the pseudo first-order kinetics in all cases. The key parameters of the fitted curves are listed in Table 2, and $k_{obs}$ is plotted as a function of SA/V in Figure 11B. As shown, a linear fitted curve was achieved ($R^2$ = 0.9948), demonstrating that $k_{obs}$ was linearly related to SA/V within certain limits, which is in accordance with previous reports [35,60,61]. The slope of this fitted line represents the specific reaction rate constant $k_{SA}$, which is the normalization of $k_{obs}$ to SA/V (i.e., $k_{SA} = k_{obs}$ normalized to SA/V) [62]. The units for $k_{obs}$ and SA/V are $s^{-1}$ and $m^{-1}$, respectively, so the unit for $k_{SA}$ should be $m{\cdot}s^{-1}$. The specific reaction rate constant $k_{SA}$ could be regarded as a general descriptor of reactivity of heterogeneous catalysts [55,62], and is calculated to be (5.9 ± 0.07) × $10^{-9}$ $m{\cdot}s^{-1}$ in this work. Judging from the $k_{obs}$ data obtained in this work, much more rapid degradation of Rh B is achieved in the presence of the proposed catalyst compared with many other conventional ones like CuO nanowires, CuO nanoparticles, CuO nanoflowers, and commercial CuO [63,64].

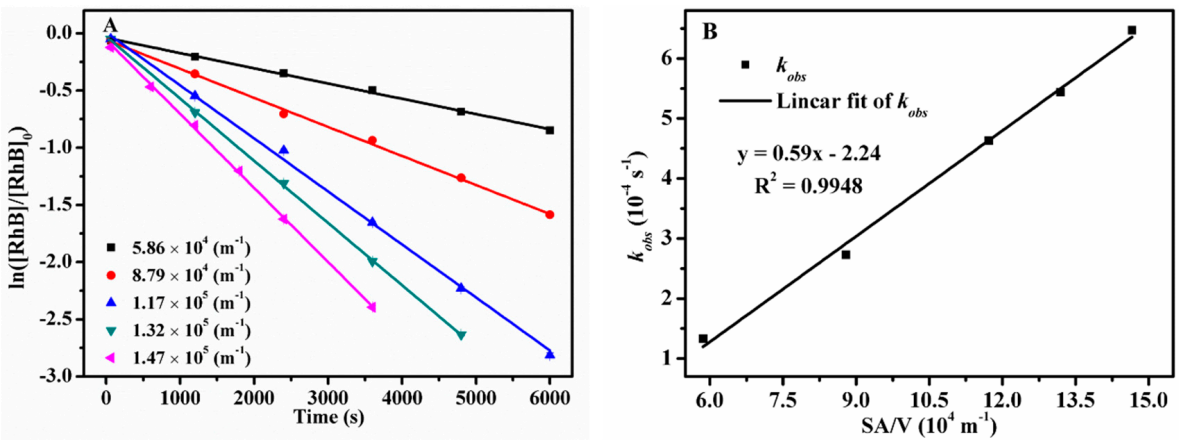


**Figure 11.** (**A**) ln([Rh B]/[Rh B]$_0$) as a function of reaction time with different surface area concentrations (5.86–14.66 × $10^4$ $m^{-1}$). Reaction conditions: [Rh B]$_0$ = 20 mg/L, [$H_2O_2$]$_0$ = 10 mM, V = 100 mL, T = 25 °C, pH 4.9 (unadjusted). (**B**) $k_{obs}$ as a function of SA/V. The $k_{obs}$ values were obtained from Figure 11A.

**Table 2.** The key parameters of the fitted curves in Figure 11A.

| Catalyst Dose (g/L) | SA/V ($10^5$ $m^{-1}$) | $k_{obs}$ ($10^{-4}$ $s^{-1}$) | Standard Deviation ($10^{-5}$ $s^{-1}$) | $R^2$ (%) |
|---|---|---|---|---|
| 0.4 | 0.586 | 1.33 | 0.317 | 99.72 |
| 0.6 | 0.879 | 2.73 | 0.592 | 99.73 |
| 0.8 | 1.172 | 4.63 | 0.859 | 99.83 |
| 0.9 | 1.319 | 5.44 | 0.409 | 99.98 |
| 1.0 | 1.466 | 6.47 | 1.042 | 99.87 |

### 2.2.7. Activation Energy

Generally, the activation energy ($E_a$) of the reaction could be calculated by the Arrhenius equation: $k_{obs} = k_1{\cdot}e^{-E_a/RT}$, which can be integrated as

$$ln(k_{obs}) = \frac{-E_a}{RT} + ln(k_1) \quad (6)$$

where $E_a$, R, and T represent the activation energy for the reaction, the gas constant, and the absolute temperature, respectively [35]. To estimate the activation energy of the reaction, a series of experiments were conducted at different temperatures from 20 to 40 °C. The ln([Rh B]/[Rh B]$_0$) was plotted as a function of time in Figure 12A to obtain $k_{obs}$ at different temperatures. The key parameters of the fitted curves were listed in Table 3, and ln($k_{obs}$) was plotted as a function of 1/T (K$^{-1}$) in Figure 12B to obtain $E_a$.

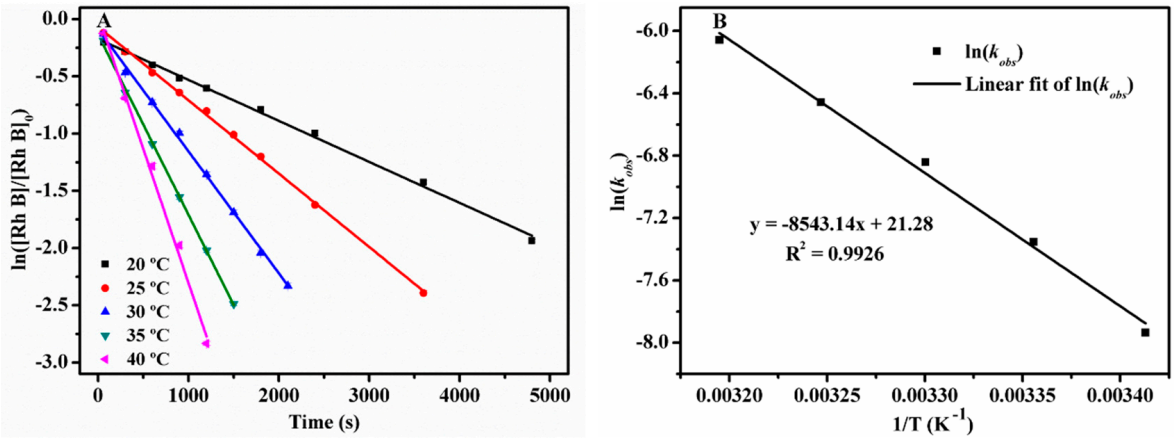


**Figure 12.** (**A**) ln([Rh B]/[Rh B]$_0$) as a function of reaction time at different temperatures (20–40 °C) in the presence of 1 g/L of the Cu/$Al_2O_3$/CN composite. Reaction conditions: [Rh B]$_0$ = 20 mg/L, [$H_2O_2$]$_0$ = 10 mM, V = 100 mL, pH 4.9 (unadjusted). (**B**) ln($k_{obs}$) as a function of 1/T. The $k_{obs}$ values are obtained from Figure 12A.

**Table 3.** The key parameters of the fitted curves in Figure 12A.

| Temperature (°C) | $k_{obs}$ ($10^{-3}$ s$^{-1}$) | Standard Deviation ($10^{-5}$ s$^{-1}$) | R$^2$ (%) |
|---|---|---|---|
| 20 | 0.358 | 0.689 | 99.70 |
| 25 | 0.647 | 1.042 | 99.87 |
| 30 | 1.07 | 2.184 | 99.71 |
| 35 | 1.57 | 2.081 | 99.91 |
| 40 | 2.34 | 8.081 | 99.53 |

As can be seen from Figure 12A, with the increase of temperature, the degradation rate of Rh B increased significantly. In addition, all the ln([Rh B]/[Rh B]$_0$) plots were linearly fitted with reaction time, reconfirming the pseudo first-order kinetics at different temperatures. The ln($k_{obs}$) is linearly fitted with 1/T with an R$^2$ of 0.9926 as shown in Figure 12B. According to the Arrhenius equation, the slope of this fitting curve equals to $-E_a$/R, and the activation energy $E_a$ was calculated to be 71.0 kJ/mol. This value was lower than a series of other similar reactions, such as the degradation of Congo red by Fenton reagent (85.9 kJ/mol), the degradation of phenol by diamond supported gold nanoparticles (90.0 kJ/mol), and the iron oxide coating Fenton-like catalyst (96.9 kJ/mol) [65–67].

### 2.2.8. Recycling Experiments

In order to evaluate the stability of the Cu/$Al_2O_3$/CN composite, recycling experiments were performed. After each cycle, the suspension was filtered, washed, and dried to obtain the remaining composite. The recovered composite was subsequently subjected to a second cycle under the same reaction conditions. The leaching of copper species was measured at the end of each reaction cycle. The results are presented in Figure 13 and Table 4. Despite that the reaction rate constant decreased to some extent, efficient removal of Rh B was still achieved with a degradation ratio of 89.7% in 50 min after four cycles with a $k_{obs}$ value of 0.77 × $10^{-3}$ s$^{-1}$, indicating that the catalytic property of the composite was efficient and long-lasting. The slight decline in catalytic performance may be attributed

to the loss of Cu species in catalyst. The leaching of copper species increased from 0.16 mg/L in the first cycle to 0.55 mg/L in the fourth cycle, which shows an increasing trend. This could be regarded as a shortcoming of the proposed catalyst, and it also provides a direction for further improvement. It is remarkable that, despite the fact that copper leaching increases with cycle numbers, only 0.55 mg/L copper species were released to the solution even after four reaction cycles, i.e., copper leaching was remained at a very low level, which is far below the European standard of effluent (2 mg/L) [48].

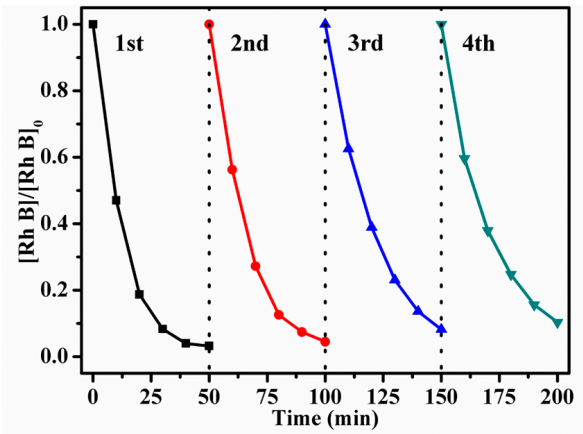


**Figure 13.** Recycling performance of the $Cu/Al_2O_3/CN$ composite for Rh B degradation in the presence of 1 g/L of the $Cu/Al_2O_3/CN$ composite. Reaction conditions: $[Rh\ B]_0$ = 10 mg/L, $[H_2O_2]_0$ = 10 mM, V = 100 mL, 25 °C, pH 4.9 (unadjusted).

**Table 4.** $k_{obs}$ and Cu leaching in the recycling experiments.

| Recycling Cycles | 1st | 2nd | 3rd | 4th |
|---|---|---|---|---|
| Removal ratio | 96.8% | 95.5% | 91.8% | 89.7% |
| $k_{obs}$ ($10^{-3}$ $s^{-1}$) | 1.37 | 1.12 | 0.83 | 0.77 |
| Cu leaching (mg/L) | 0.16 | 0.37 | 0.43 | 0.55 |

In some systems the dissolved metal species could form certain complexes that are able to catalyze the decomposition of $H_2O_2$, thereby persistently generating HO· [36,68]. To determine the effect of dissolved copper species on Rh B degradation, the suspension containing $Cu/Al_2O_3/CN$ composite was filtered at 40 min to remove catalyst particles, and the residual Rh B in the filtrate was monitored over time. As shown in Figure S2, negligible Rh B degradation was observed in the filtrate, indicating that the dissolved copper species had little effect on Rh B degradation, so only surface reaction dominates in the system containing the $Cu/Al_2O_3/CN$ composite. With a tiny loss of copper species, the $Cu/Al_2O_3/CN$ composite remains highly reactive and could efficiently catalyze the degradation of Rh B. The main features of the proposed $Cu/Al_2O_3/CN$ composite and some other copper-based Fenton-like catalysts on Rh B degradation are listed in Table S1 [27,40,48,63,64,69–73]. The superiority of the $Cu/Al_2O_3/CN$ composite in this work is supported by its high degradation rate constant, low copper leaching, and excellent applicability in neutral and alkaline conditions.

### *2.3. Catalytic Mechanism*

In order to ascertain the Rh B degradation mechanism by the $Cu/Al_2O_3/CN$ composite, both the reactive species and degradation products were identified in the Rh B degradation process. The reactive species were identified by a radical scavenger and ESR analysis, and HPLC-MS analysis was used to separate the degradation products and to identify each component. A tentative mechanism was proposed based on the abovementioned results.

### 2.3.1. Scavenging Experiments

Isopropanol (IPA) was employed as the HO· scavenger due to its rapid reaction rate with HO· ($1.9 \times 10^{-9}$ $M^{-1} \cdot s^{-1}$) [38]. As shown in Figure 14A, by increasing the IPA concentration from 10 to 100 mM, the scavenging effect became more significant, which indicates that HO· radical is the primary oxidation species in the catalytic reaction. This conclusion is also supported by the ESR experiment in which different radicals were trapped by DMPO to form different adducts that have different spectra [74,75]. As shown in Figure 14B, no ESR signal was observed in the absence of $H_2O_2$. With the addition of $H_2O_2$, a four-line ESR signal was observed with the relative intensity of 1:2:2:1, which is the characteristic spectrum of the DMPO-HO· adduct. This result reconfirmed the existence of HO· as main reactive species. Additionally, the characteristic spectrum of DMPO-$O_2{\cdot}^-$ with a relative intensity of 1:1:1:1 was also observed in Figure 14C. $O_2{\cdot}^-$ may arise from the reaction between HO· and $H_2O_2$ as shown in Equation (4). Notably, the intensity of the DMPO-HO· signal reached maximum at 10 min, while the intensity of DMPO-$O_2{\cdot}^-$ signal continuously increased over time, which supports that the observed $O_2{\cdot}^-$ radicals were generated from HO· radicals.

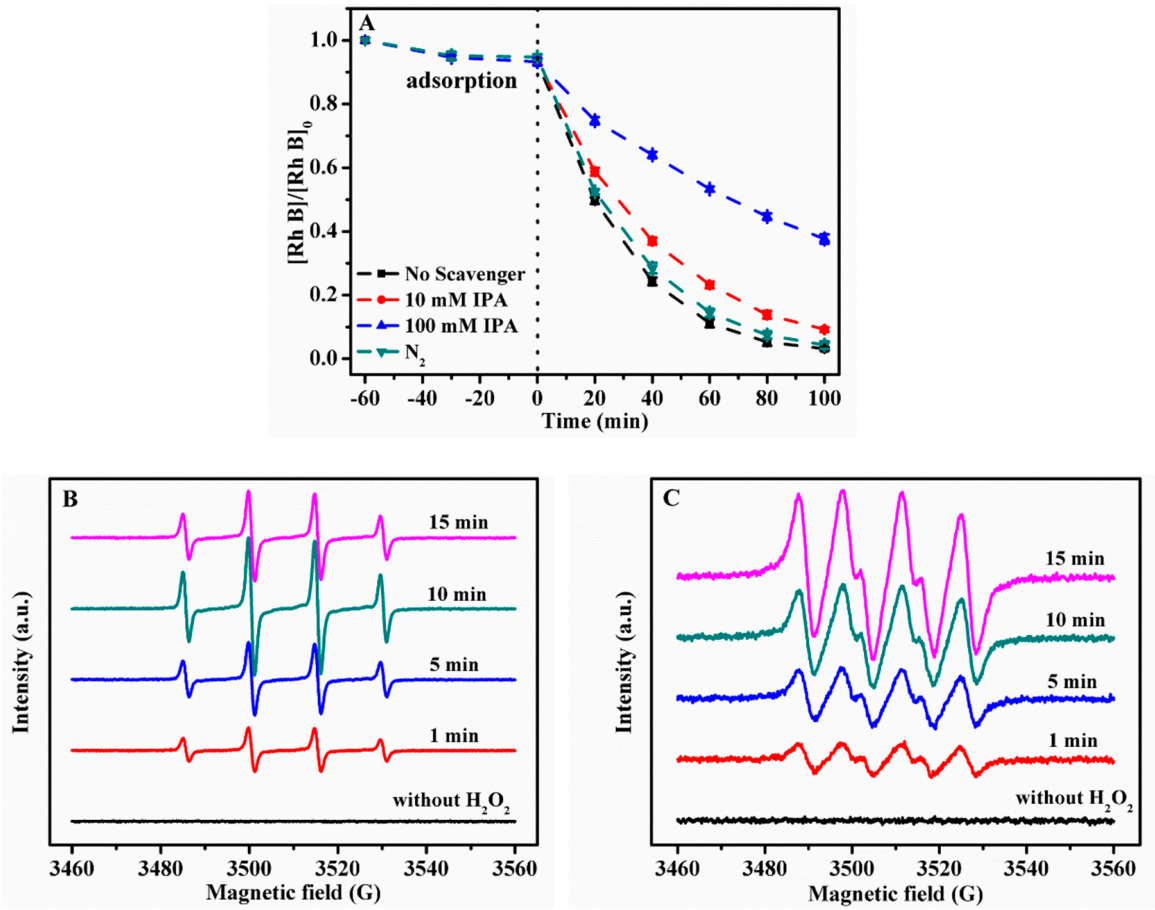


**Figure 14.** (**A**) [Rh B]/[Rh B]$_0$ as a function of time in the presence of different concentrations of IPA and $N_2$ bubbling. ESR spectra of (**B**) DMPO-HO· adducts in aqueous solution and (**C**) DMPO-$O_2{\cdot}^-$ adducts in methanol solution recorded with the Cu/$Al_2O_3$/CN composite.

Moreover, the effect of dissolved oxygen on Rh B degradation was checked by $N_2$ bubbling. The Rh B solution was purged by $N_2$ for 30 min before the reaction to dissipate dissolved oxygen. As shown in Figure 14A, the presence and absence of dissolved oxygen exerted no significant influences on Rh B degradation, indicating that oxygen was not the source of HO·, and the HO· radicals mainly arose from $H_2O_2$. In summary, HO· was identified as the major reactive species generated in the reaction, and the $O_2{\cdot}^-$ was generated via the reaction of HO· and $H_2O_2$.

### 2.3.2. HPLC-MS Analysis

Since HO· was confirmed as the main contributing reactive species, the $Cu/Al_2O_3/CN$ system exhibited a universal degradation peroperty for other organic pollutants as expected. As shown in Figure S3, the degradation ratios of methyl orange (MO), Rh B, and methylene blue (MB) in 100 min were 55.3%, 96.4%, and 93.1%, respectively. Particularly, the degradation products of Rh B were identified by HPLC-MS analysis.

The HPLC chromatograms of samples extracted at different reaction times were recorded in Figure S4. The two main peaks at 14.7 and 16.9 min corresponded to N-de-ethylated intermediate and Rh B, respectively, which were confirmed by MS identification [76]. It is clear that the peak of Rh B decreased with time, which was accompanied with the formation and subsequent elimination of other peaks. This implies that some transformation products were formed in the degradation process, and these produced compounds were further degraded into smaller products.

Based on the results above and previous reports [76–79], the possible degradation pathways of Rh B are proposed in Figure 15, which could be mainly summarized as N-de-ethylation, chromophore cleavage, ring opening and mineralization process. The MS spectra of each product were shown in Figure S5. A compound with a *m/z* value of 443 was identified to be Rh B, and the intermediates with *m/z* values of 415 and 387 were identified as N, N-diethyl-N′-ethyl rhodamine (DER), and N, N-diethyl rhodamine (DR), respectively. The intermediates with the *m/z* value of 387 could also be N-ethyl-N′-ethyl rhodamine (EER), which is the isomer of DR and has an ethyl on each side. These intermediates prove that in the first stage Rh B was degraded through a stepwise N-de-ethylation pathway, which finally forms an intermediate with an *m/z* value of 318 [79]. At the same time, the de-carboxylation process occurs and forms the product with a *m/z* value of 274 [80], and the central carbon of Rh B was also attacked by HO· radicals to form the hydroxylated product (*m/z* = 459) via the additive reaction [78]. There were two unidentified peaks with m/z values of 453 and 475, which could be regarded as the $[M + H]^+$ and $[M + Na]^+$ adducts of an unknown intermediate. To the best of our knowledge, no such pseudomolecule ion with m/z = 453 was previously reported in Rh B degradation, and we deemed that this compound might not exert a significant influence on the whole degradation pathway. Thus, it is marked unidentified in the present work. In the next stage, non-selective HO· directly attacks the center carbon of these N-de-ethylated intermediates, leading to the cleavage of the conjugated xanthene structure [81]. The intermediates with *m/z* values of 340, 245, 230, and 223 were identified from this process [82–85]. After the chromophore cleavage process, the ring opening process occurs and forms smaller molecules. The ring opening products such as tricarballylic acid, 7-oxooctanoic acid, and propionic acid with m/z values of 177, 158, and 74 were identified [81]. In the final stage, these small molecules were possibly mineralized to $CO_2$, $H_2O$, $NO_3^-$, $NH_4^+$, etc.

Based on the results and analysis above, a tentative mechanism for the catalytic performance of the $Cu/Al_2O_3/CN$ composite was proposed. Copper species were bonded to the $Al_2O_3$ framework, which facilitates the conversion of $H_2O_2$ to HO· by Fenton-like reaction and broadens the pH range for application. CN provides a large surface area and multiple functional groups to load $Cu/Al_2O_3$ composite by the formation of C−O−Cu bonds. In the presence of the $Cu/Al_2O_3/CN$ composite, aqueous $H_2O_2$ could be easily adsorbed to the surface of CN, increasing its chance to contact with immobilized copper species to generate HO·. The catalytic process is surface predominant and the tiny leaching of copper species leads to an efficient and long-lasting catalytic property. $O_2{\cdot}^-$ is generated via the reaction of HO· and $H_2O_2$, and the highly reactive HO· attacks Rh B molecules, leading to the degradation of Rh B into smaller molecules.

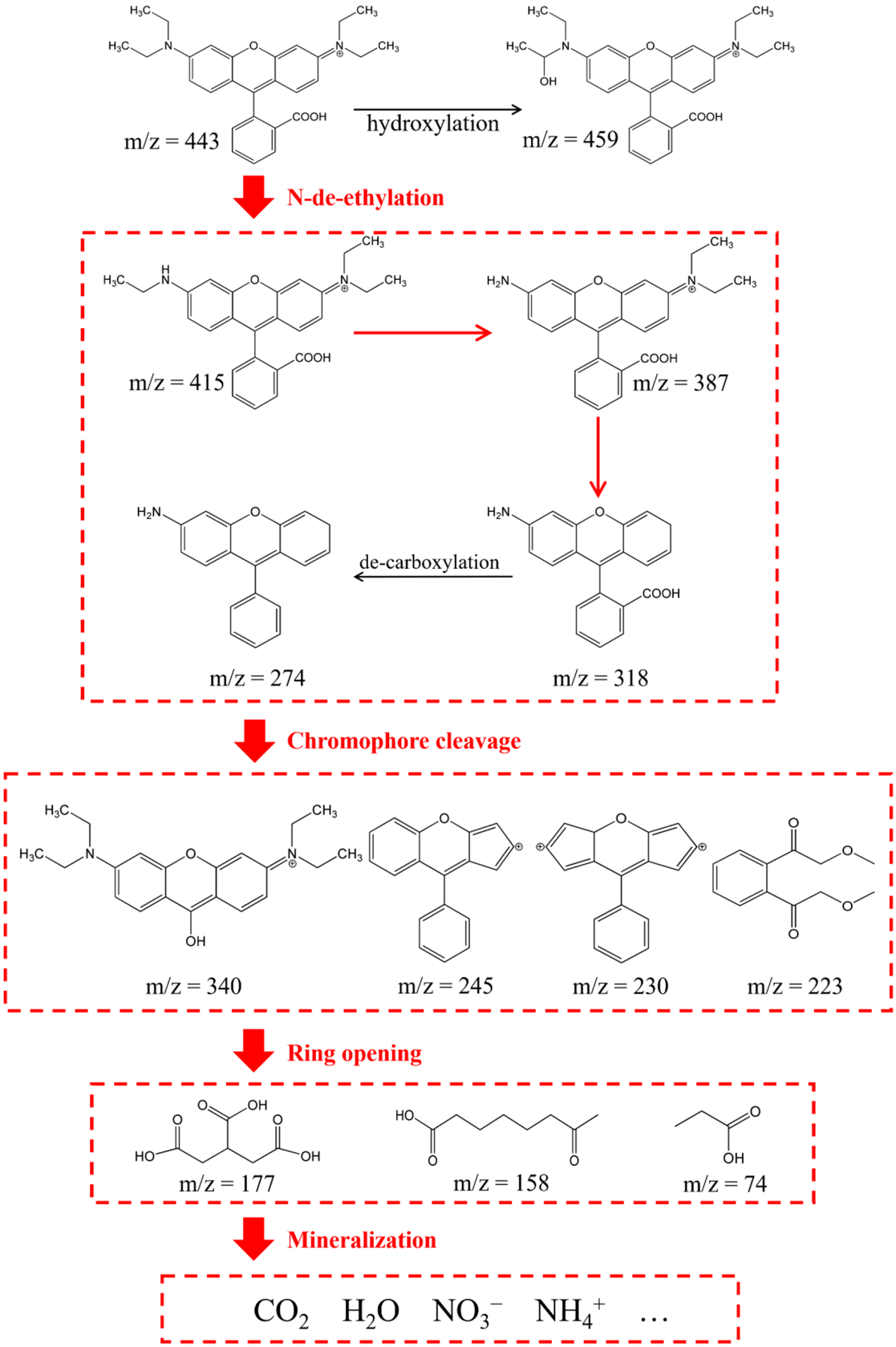


**Figure 15.** Illustration of the proposed Rh B degradation pathways.

## 3. Experimental

### *3.1. Materials*

The chemicals used in the present work included aluminum nitrate nonahydrate ($Al(NO_3)_3{\cdot}9H_2O$, CAS[7784-27-2], 99%), copper(II) nitrate trihydrate ($Cu(NO_3)_3{\cdot}3H_2O$, CAS[10031-43-3], 99%), D(+)−glucose monohydrate ($C_6H_{12}O_6{\cdot}H_2O$, CAS[14431-43-7], 99%), urea ($CH_4N_2O$, CAS[57-13-6], 99%), Rhodamine B (Rh B, $C_{28}H_{31}ClN_2O_3$, CAS[81-88-9], 99.7%), methylene blue trihydrate (MB, $C_{16}H_{16}ClN_3S{\cdot}3H_2O$, CAS[7720-79-3], 82%), methyl orange (MO, $C_{14}H_{14}N_3NaO_3S$, CAS[547-58-0], 98.5%), hydrogen peroxide ($H_2O_2$, CAS[7722-84-1], 30 wt %), potassium iodide (KI, CAS[7681-11-0], 99%), acetic acid ($C_2H_4O_2$, CAS[64-19-7], 99.5%), sodium acetate anhydrous ($CH_3COONa$, CAS[127-09-3], 99%), isopropanol (IPA, $C_3H_8O$, CAS[67-63-0], 99.7%) (Sinopharm, Beijing, China), and ammonium molybdate (di) ($(NH_4)_2Mo_2O_7$, CAS[27546-07-2], Mo 56.5%, Macklin, Shanghai, China). All chemicals were used without further purification. All the solutions were prepared in deionized water.

### *3.2. Preparation of Composites*

#### 3.2.1. Preparation of $Cu/Al_2O_3$

$Cu/Al_2O_3$ composite was prepared via a hydrothermal method followed by a calcination process [40]. Typically, 7.5 g of $Al(NO_3)_3{\cdot}9H_2O$, 5.0 g of $C_6H_{12}O_6$, 0.9 g of $Cu(NO_3)_2{\cdot}3H_2O$, and 60 mL of ultrapure water were added to a 100 mL breaker, and stirred at 25 °C for 1 h. The solution was transferred into a 100 mL Teflon-lined autoclave, then heated to 180 °C and kept for 20 h in an oven. After suction filtering, and water washing to neutral, the obtained product was added to an alumina crucible with a cover and then heated to 550 °C with a ramping rate of 5 °C/min in a muffle furnace and hold at 550 °C for 4 h. After naturally cooling down to room temperature, the product $Cu/Al_2O_3$ was obtained, and labeled as $Cu_{12}/Al_2O_3$, where 12 represents the initial mass ratio of $Cu(NO_3)_2{\cdot}3H_2O$ to $Al(NO_3)_3{\cdot}9H_2O$ in percentage. Following the same procedure, a series of $Cu_x/Al_2O_3$ composites (x = 4, 7, 9, 12, and 15 wt %) were prepared in order to obtain the optimal Cu content.

#### 3.2.2. Preparation of g-$C_3N_4$

Pure g-$C_3N_4$ was prepared following the thermal polymerization process reported in a previous study [35]. Typically, 50 g of urea was added to an alumina crucible with a cover and then heated to 550 °C with a ramping rate of 5 °C/min in a muffle furnace and hold at 550 °C for 3 h. After naturally cooling down to room temperature, the product g-$C_3N_4$ was obtained, and labeled as CN.

#### 3.2.3. Preparation of $Cu/Al_2O_3/CN$

The $Cu/Al_2O_3/CN$ composite was prepared using the samples obtained in Sections 3.2.1 and 3.2.2. Typically, 0.1 g of the $Cu_{12}/Al_2O_3$ composite and 0.1 g of CN were immersed in 100 mL ultrapure water. The suspension was dispersed by ultrasound for 30 min. After drying at 80 °C and grinding to powder, the product $Cu/Al_2O_3/CN$ composite was obtained, and labeled as $Cu_{12}/Al_2O_3/CN_{1.3}$, where 1.3 represents the initial mass ratio of CN to $Al(NO_3)_3{\cdot}9H_2O$ in percentage. Additionally, a series of $Cu_{12}/Al_2O_3/CN_y$ composites (y = 0.7, 1.3, 2.0, and 2.7 wt %) were prepared by the same synthetic process to obtain the optimal CN content.

### *3.3. Characterization of Prepared Composites*

The Fourier transform infrared (FT-IR) spectra of prepared samples were recorded by a Nicolet iS5 (Thermo Fisher Scientific, Waltham, MA., USA) FT-IR spectrometer with KBr pellets to confirm the functional groups of materials.

X-ray diffraction (XRD) patterns were recorded with D8 advance (Bruker, Karlsruhe, Germany) diffractometer using Bragg–Brentano geometry over the 2θ range of 10–70° with a Cu Kα irradiation (λ = 1.54 Å) to obtain the crystal structure of materials.

The morphology of the synthesized samples was visualized by a JET-2100F (JEOL, Akishima, Japan) transmission electron microscope (TEM).

X-ray photoelectron spectroscopy (XPS) data was recorded at 100 W power with a 20 eV pass energy on an ESCALAB 250Xi instrument (Thermo Fisher Scientific, Waltham, MA., USA).

The Brunauer–Emmett–Teller (B.E.T) method via isothermal adsorption and desorption of high purity nitrogen using a TriStar II 3020 (Micromeritics, Norcross, GA., USA) instrument was used to determine the specific surface area of synthesized samples.

The degradation intermediates were identified by a high performance liquid chromatography-mass spectrometry (HPLC-MS, thermo TSQ Quantum Ultra, Waltham, MA., USA). The samples were chromatographically separated by a 2.1 mm × 150 mm XB C18 column with a particle size of 3 μm (Welch, Shanghai, China) with acetonitrile/0.1% formic acid (8:92, *v*/*v*) as the mobile phase The flow rate was 0.3 mL/min and the injection volume was 20 μL. The eluent was detected by a diode array detector at the wavelength of 555 nm. The total ion current was recorded by quadrupole in a positive mode with electrospray ionization as ion source.

The concentration of the dissolved copper species was measured by a Prodigy 7 (Teledyne Leeman Labs, Hudson, NH., USA) inductively coupled plasma-optical emission spectrometer (ICP-OES).

The electron spin resonance (ESR) signals of radicals spin-trapped by 5,5-dimethyl-pyrroline-N-oxide (DMPO) were detected by a Bruker/A300 spectrometer (Bruker, Karlsruhe, Germany) with or without the addition of $H_2O_2$ in different air saturated methanol/aqueous dispersions.

The concentration of $H_2O_2$ and Rh B was measured by the UV-5500PC UV-visible spectrophotometer (METASH, Shanghai, China) and V-5600 spectrophotometer (METASH, Shanghai, China). The samples were weighted using a ME204E microbalance (Mettler Toledo, Shanghai, China). The pH of the solution was measured by Starter 2100 pH meter (Ohaus, Shanghai, China) with an accuracy of ± 0.01 pH units.

### *3.4. Catalytic Experiments*

Rh B was selected to evaluate the catalytic performance of the synthesized samples. All experiments were performed in dark conditions. Typically, 0.1 g of sample was placed into 100 mL of 20 mg/L Rh B solution, and then the suspension was stirred continuously for 1 h prior to the addition of $H_2O_2$, in order to achieve Rh B adsorption/desorption equilibrium. Afterwards, predetermined amount of $H_2O_2$ was added in the suspension under constant stirring to trigger the reaction. At given time intervals, 4 mL samples were collected with a syringe and filtered using a Millipore filter (220 nm, Tianjin, China). The concentrations of Rh B and $H_2O_2$ in the filtrate were measured and plotted as a function of time.

The concentrations of Rh B and $H_2O_2$ in solutions were measured using a UV-visible spectrophotometer due to its convenience and easy operation. The produced intermediates may interfere the measurements, but the experimental error in the determination of Rh B and $H_2O_2$ concentration was less than 2%, which is acceptable for subsequent discussions. Generally, the absorbance of Rh B was measured at 555 nm in which Rh B had the maximum absorption. The concentration of $H_2O_2$ was determined by the Ghormley triiodide method reported in previous work [68]. The $I^-$ could be oxidized by $H_2O_2$ to form $I_3^-$ in the presence of catalyst $(NH_4)_2Mo_2O_7$ (ADM). The $I_3^-$ has the maximum absorption peak at the wavelength of 350 nm, thus the standard curve of the absorbance of $I_3^-$ as a function of $H_2O_2$ concentration can be obtained.

Radical scavenger experiments were carried out to investigate the reactive oxygen species in the system. The scavenger IPA was added into the suspension after the adsorption/desorption equilibrium prior to the addition of $H_2O_2$. Additionally, Rh B solution was purged with $N_2$ prior to the addition of composite to exclude $O_2$.

## 4. Conclusions

An efficient Fenton-like $Cu/Al_2O_3/CN$ composite was proposed in this work. The characterizations show that Cu species were immobilized on the $Al_2O_3$ framework in the form of $Cu^{2+}$ and $Cu^{+}$, and the introduction of CN increases its specific surface area and adsorption capacity for Rh B. The $Cu/Al_2O_3/CN$ composite showed an excellent catalytic performance in a wide range of pH (4.9–11.0). The specific reaction rate constant of Rh B degradation was calculated as $(5.9 \pm 0.07) \times 10^{-9}$ m·s$^{-1}$, and the activation energy was calculated to be 71.0 kJ/mol. The recycling experiment demonstrated its durability for Rh B removal and proved that the degradation reaction was surface doninated, with a negligible leaching of copper species in solution. HO· and $O_2{\cdot}^{-}$ were both major reactive oxygen species generated in the reaction, and HO· was mainly responsible for Rh B degradation, which involves N-de-ethylation, hydroxylation, de-carboxylation, chromophore cleavage, ring opening, and the mineralization process. This work shows that $Cu/Al_2O_3/CN$ composite is a promising Fenton-like catalyst with high activity and stability for the treatment of water pollution.

**Supplementary Materials:** The following are available online at http://www.mdpi.com/2073-4344/10/3/317/s1, Figure S1: (**A**) $[H_2O_2]$, (**B**) [Rh B]/$[\text{Rh B}]_0$, and (**C**) ln ([Rh B]/ $[\text{Rh B}]_0$) as a function of time in the presence of 1 g/L of the $Cu/Al_2O_3/CN$ composite at room temperature. Reaction conditions: $[\text{Rh B}]_0$ = 20 mg/L, $[H_2O_2]_0$ = 10 mM, V = 100 mL, pH 4.9 (unadjusted); Figure S2: [Rh B]/$[\text{Rh B}]_0$ as a function of time in nonfiltered $Cu/Al_2O_3/CN$ suspension and filtrates obtained at selected time intervals. Reaction conditions: [catalyst] = 1 g/L, $[\text{Rh B}]_0$ = 20 mg/L, $[H_2O_2]_0$ = 10 mM, V = 100 mL, 25 °C, pH 4.9 (unadjusted); Figure S3: $C/C_0$ as a function of time with different organic pollutants in the presence of 1 g/L of the $Cu/Al_2O_3/CN$ composite. Reaction conditions: [dye] = 20 mg/L, $[H_2O_2]_0$ = 10 mM, V = 100 mL, 25 °C, pH 4.9 (unadjusted); Figure S4: HPLC chromatograms of samples extracted at different reaction times. Reaction conditions: [catalyst] = 1 g/L, [dye] = 20 mg/L, $[H_2O_2]_0$ = 10 mM, V = 100 mL, 25 °C, pH 4.9 (unadjusted); Figure S5: Mass spectrograms of the degradation products in sample extracted at 60 min in Rh B degradation.; Table S1: Comparison of the catalytic activities of the $Cu/Al_2O_3/CN$ composite with other copper-based Fenton-like catalysts.

**Author Contributions:** M.Y. conceived the experiments; C.Z. and Z.L. designed and performed the experiments; L.F. and Y.G. analyzed the data; Y.F. contributed analysis tools; C.Z., Z.L. and M.Y. wrote the paper. All authors have read and agreed to the published version of the manuscript.

**Funding:** This work is supported by National Natural Science Foundation of China (21707108) and Independent Innovation Foundation of Wuhan University of Technology (20411057 and 20410962).

**Conflicts of Interest:** The authors declare no conflict of interest.

## References

1. Wang, J.L.; Wang, S.Z. Removal of pharmaceuticals and personal care products (PPCPs) from wastewater: A review. *J. Environ. Manag.* **2016**, *182*, 620–640. [CrossRef] [PubMed]
2. Pavithra, K.G.; Kumar, P.S.; Jaikumar, V.; Rajan, P.S. Removal of colorants from wastewater: A review on sources and treatment strategies. *J. Ind. Eng. Chem.* **2019**, *75*, 1–19. [CrossRef]
3. Li, H.P.; Liu, J.Y.; Hou, W.G.; Du, N.; Zhang, R.J.; Tao, X.T. Synthesis and characterization of g-$C_3N_4/Bi_2MoO_6$ heterojunctions with enhanced visible light photocatalytic activity. *Appl. Catal. B* **2014**, *160*, 89–97. [CrossRef]
4. Adityosulindro, S.; Barthe, L.; González-Labrada, K.; Jáuregui Haza, U.J.; Delmas, H.; Julcour, C. Sonolysis and sono-Fenton oxidation for removal of ibuprofen in (waste)water. *Ultrason. Sonochem.* **2017**, *39*, 889–896. [CrossRef] [PubMed]
5. Bai, C.P.; Xiong, X.F.; Gong, W.Q.; Feng, D.X.; Xian, M.; Ge, Z.X.; Xu, N.A. Removal of rhodamine B by ozone-based advanced oxidation process. *Desalination* **2011**, *278*, 84–90.
6. Masomboon, N.; Ratanatamskul, C.; Lu, M.C. Kinetics of 2,6-dimethylaniline oxidation by various Fenton processes. *J. Hazard. Mater.* **2011**, *192*, 347–353. [CrossRef]
7. Patil, S.P.; Bethi, B.; Sonawane, G.H.; Shrivastava, V.S.; Sonawane, S. Efficient adsorption and photocatalytic degradation of Rhodamine B dye over $Bi_2O_3$-bentonite nanocomposites: A kinetic study. *J. Ind. Eng. Chem.* **2016**, *34*, 356–363. [CrossRef]
8. Madhavan, J.; Grieser, F.; Ashokkumar, M. Combined advanced oxidation processes for the synergistic degradation of ibuprofen in aqueous environments. *J. Hazard. Mater.* **2010**, *178*, 202–208. [CrossRef]
9. Rao, Y.F.; Xue, D.; Pan, H.M.; Feng, J.T.; Li, Y.J. Degradation of ibuprofen by a synergistic UV/Fe(III)/Oxone process. *Chem. Eng. J.* **2016**, *283*, 65–75. [CrossRef]

10. Al-Hamadani, Y.A.J.; Park, C.M.; Assi, L.N.; Chu, K.H.; Hoque, S.; Jang, M.; Yoon, Y.; Ziehl, P. Sonocatalytic removal of ibuprofen and sulfamethoxazole in the presence of different fly ash sources. *Ultrason. Sonochem.* **2017**, *39*, 354–362. [CrossRef]
11. Cheng, M.; Zeng, G.M.; Huang, D.L.; Lai, C.; Xu, P.; Zhang, C.; Liu, Y. Hydroxyl radicals based advanced oxidation processes (AOPs) for remediation of soils contaminated with organic compounds: A review. *Chem. Eng. J.* **2016**, *284*, 582–598. [CrossRef]
12. Babuponnusami, A.; Muthukumar, K. A review on Fenton and improvements to the Fenton process for wastewater treatment. *J. Environ. Chem. Eng.* **2014**, *2*, 557–572. [CrossRef]
13. Saleh, R.; Taufik, A. Degradation of methylene blue and congo-red dyes using Fenton, photo-Fenton, sono-Fenton, and sonophoto-Fenton methods in the presence of iron (II,III) oxide/zinc oxide/graphene ($Fe_3O_4$/ZnO/graphene) composites. *Sep. Purif. Technol.* **2019**, *210*, 563–573. [CrossRef]
14. Bello, M.M.; Raman, A.A.A.; Asghar, A. A review on approaches for addressing the limitations of Fenton oxidation for recalcitrant wastewater treatment. *Process Saf. Environ. Prot.* **2019**, *126*, 119–140. [CrossRef]
15. Wang, P.; Wang, N.N.; Zheng, T.; Zhang, G.S. A review on Fenton-like processes for organic wastewater treatment. *J. Environ. Chem. Eng.* **2016**, *4*, 762–787. [CrossRef]
16. de Luna, M.D.G.; Colades, J.I.; Su, C.C.; Lu, M.C. Comparison of dimethyl sulfoxide degradation by different Fenton processes. *Chem. Eng. J.* **2013**, *232*, 418–424. [CrossRef]
17. Karpinska, A.; Sokol, A.; Karpinska, J. Studies on the kinetics of carbamazepine degradation in aqueous matrix in the course of modified Fenton's reactions. *J. Pharm. Biomed. Anal.* **2015**, *106*, 46–51. [CrossRef]
18. Yamaguchi, R.; Kurosu, S.; Suzuki, M.; Kawase, Y. Hydroxyl radical generation by zero-valent iron/Cu (ZVI/Cu) bimetallic catalyst in wastewater treatment: Heterogeneous Fenton/Fenton-like reactions by Fenton reagents formed in-situ under oxic conditions. *Chem. Eng. J.* **2018**, *334*, 1537–1549. [CrossRef]
19. Xia, D.H.; Xu, W.J.; Hu, L.L.; He, C.; Leung, D.Y.C.; Wang, W.J.; Wong, P.K. Synergistically catalytic oxidation of toluene over Mn modified g-$C_3N_4$/ZSM-4 under vacuum UV irradiation. *J. Hazard. Mater.* **2018**, *349*, 91–100. [CrossRef]
20. Su, Y.H.; Chen, P.; Wang, F.L.; Zhang, Q.X.; Chen, T.S.; Wang, Y.F.; Yao, K.; Lv, W.Y.; Liu, G.G. Decoration of $TiO_2$/g-$C_3N_4$ Z-scheme by carbon dots as a novel photocatalyst with improved visible-light photocatalytic performance for the degradation of enrofloxacin. *RSC Adv.* **2017**, *7*, 34096–34103. [CrossRef]
21. Nieto-Juarez, J.I.; Pierzchla, K.; Sienkiewicz, A.; Kohn, T. Inactivation of $MS_2$ coliphage in Fenton and Fenton-like systems: Role of transition metals, hydrogen peroxide and sunlight. *Environ. Sci. Technol.* **2010**, *44*, 3351–3356. [CrossRef] [PubMed]
22. Zhang, L.L.; Xu, D.; Hu, C.; Shi, Y.L. Framework Cu-doped $AlPO_4$ as an effective Fenton-like catalyst for bisphenol A degradation. *Appl. Catal. B* **2017**, *207*, 9–16. [CrossRef]
23. Li, Z.F.; Soroka, I.L.; Min, F.Y.; Jonsson, M. pH-Control as a way to fine-tune the Cu/$Cu_2O$ ratio in radiation induced synthesis of $Cu_2O$ particles. *Dalton Trans.* **2018**, *47*, 16139–16144. [CrossRef] [PubMed]
24. Zhang, L.; Wu, B.D.; Zhang, G.Y.; Gan, Y.H.; Zhang, S.J. Enhanced decomplexation of Cu(II)-EDTA: The role of acetylacetone in Cu-mediated photo-Fenton reactions. *Chem. Eng. J.* **2019**, *358*, 1218–1226. [CrossRef]
25. Xu, J.H.; Wang, W.Z.; Gao, E.P.; Ren, J.; Wang, L. $Bi_2WO_6$/Cu-0: A novel coupled system with enhanced photocatalytic activity by Fenton-like synergistic effect. *Catal. Commun.* **2011**, *12*, 834–838. [CrossRef]
26. Mao, J.; Quan, X.; Wang, J.; Gao, C.; Chen, S.; Yu, H.T.; Zhang, Y.B. Enhanced heterogeneous Fenton-like activity by Cu-doped $BiFeO_3$ perovskite for degradation of organic pollutants. *Front. Environ. Sci. Eng. Chin.* **2018**, *12*, 1–10. [CrossRef]
27. Zhang, L.L.; Nie, Y.L.; Hu, C.; Qu, J.H. Enhanced Fenton degradation of Rhodamine B over nanoscaled Cu-doped $LaTiO_3$ perovskite. *Appl. Catal. B* **2012**, *125*, 418–424. [CrossRef]
28. Xiao, P.; Li, H.L.; Wang, T.; Xu, X.L.; Li, J.L.; Zhu, J.J. Efficient Fenton-like La-Cu-O/SBA-15 catalyst for the degradation of organic dyes under ambient conditions. *RSC Adv.* **2014**, *4*, 12601–12604. [CrossRef]
29. Bonfim, D.P.F.; Santana, C.S.; Batista, M.S.; Fabiano, D.P. Catalytic Evaluation of CuO/[Si]MCM-41 in Fenton-like Reactions. *Chem. Eng. Technol.* **2019**, *42*, 882–888. [CrossRef]
30. Zuo, S.Y.; Xu, H.M.; Liao, W.; Yuan, X.J.; Sun, L.; Li, Q.; Zan, J.; Li, D.Y.; Xia, D.S. Molten-salt synthesis of g-$C_3N_4$-$Cu_2O$ heterojunctions with highly enhanced photocatalytic performance. *Colloids Surf. A* **2018**, *546*, 307–315. [CrossRef]

31. Peng, B.Y.; Zhang, S.S.; Yang, S.Y.; Wang, H.J.; Yu, H.; Zhang, S.Q.; Peng, F. Synthesis and characterization of g-$C_3N_4$/$Cu_2O$ composite catalyst with enhanced photocatalytic activity under visible light irradiation. *Mater. Res. Bull.* **2014**, *56*, 19–24. [CrossRef]
32. Liu, Q.; Guo, Y.R.; Chen, Z.H.; Zhang, Z.G.; Fang, X.M. Constructing a novel ternary Fe(III)/graphene/g-$C_3N_4$ composite photocatalyst with enhanced visible-light driven photocatalytic activity via interfacial charge transfer effect. *Appl. Catal. B* **2016**, *183*, 231–241. [CrossRef]
33. Pomilla, F.R.; Cortes, M.A.L.R.M.; Hamilton, J.W.J.; Molinari, R.; Barbieri, G.; Marci, G.; Palmisano, L.; Sharma, P.K.; Brown, A.; Byrne, J.A. An Investigation into the Stability of Graphitic $C_3N_4$ as a Photocatalyst for $CO_2$ Reduction. *J. Phys. Chem. C* **2018**, *122*, 28727–28738. [CrossRef]
34. Liu, J.; Liu, Y.; Liu, N.Y.; Han, Y.Z.; Zhang, X.; Huang, H.; Lifshitz, Y.; Lee, S.T.; Zhong, J.; Kang, Z.H. Metal-free efficient photocatalyst for stable visible water splitting via a two-electron pathway. *Science* **2015**, *347*, 970–974. [CrossRef] [PubMed]
35. Liu, Z.D.; Shen, Q.M.; Zhou, C.S.; Fang, L.J.; Yang, M.; Xia, T. Kinetic and Mechanistic Study on Catalytic Decomposition of Hydrogen Peroxide on Carbon-Nanodots/Graphitic Carbon Nitride Composite. *Catalysts* **2018**, *8*, 445. [CrossRef]
36. Fang, L.J.; Liu, Z.D.; Zhou, C.S.; Guo, Y.L.; Feng, Y.P.; Yang, M. Degradation Mechanism of Methylene Blue by $H_2O_2$ and Synthesized Carbon Nanodots/Graphitic Carbon Nitride/Fe(II) Composite. *J. Phys. Chem. C* **2019**, *123*, 26921–26931. [CrossRef]
37. Lyu, L.; Zhang, L.L.; He, G.Z.; He, H.; Hu, C. Selective $H_2O_2$ conversion to hydroxyl radicals in the electron-rich area of hydroxylated C-g-$C_3N_4$/ CuCo-$Al_2O_3$. *J. Mater. Chem. A* **2017**, *5*, 7153–7164. [CrossRef]
38. Zhu, J.J.; Xiao, P.; Li, H.L.; Carabineiro, S.A.C. Graphitic Carbon Nitride: Synthesis, Properties, and Applications in Catalysis. *ACS Appl. Mater. Interfaces* **2014**, *6*, 16449–16465. [CrossRef]
39. Jia, J.K.; Huang, W.X.; Feng, C.S.; Zhang, Z.; Zuojiao, K.C.; Liu, J.X.; Jiang, C.Y.; Wang, Y.P. Fabrication of g-$C_3N_4$/$Ag_3PO_4$-$H_2O_2$ heterojunction system with enhanced visible-light photocatalytic activity and mechanism insight. *J. Alloys Compd.* **2019**, *790*, 616–625. [CrossRef]
40. Xu, S.Q.; Zhu, H.X.; Cao, W.R.; Wen, Z.B.; Wang, J.N.; Francois-Xavier, C.P.; Wintgens, T. Cu-$Al_2O_3$-g-$C_3N_4$ and Cu-$Al_2O_3$-C-dots with dual-reaction centres for simultaneous enhancement of Fenton-like catalytic activity and selective $H_2O_2$ conversion to hydroxyl radicals. *Appl. Catal. B* **2018**, *234*, 223–233. [CrossRef]
41. Xu, D.; Zhang, L.L.; Liu, L.F. Fenton-like Catalytic Removal of Organic Pollutants in Water by Framework Cu in Cu-$Al_2O_3$. *Huanjing Kexue* **2017**, *38*, 1054–1060.
42. Ma, X.Z.; Zhang, J.T.; Wang, B.; Li, Q.G.; Chu, S. Hierarchical $Cu_2O$ foam/g-$C_3N_4$ photocathode for photoelectrochemical hydrogen production. *Appl. Surf. Sci.* **2018**, *427*, 907–916. [CrossRef]
43. Dikdim, J.M.D.; Gong, Y.; Noumi, G.B.; Sieliechi, J.M.; Zhao, X.; Ma, N.; Yang, M.; Tchatchueng, J.B. Peroxymonosulfate improved photocatalytic degradation of atrazine by activated carbon/graphitic carbon nitride composite under visible light irradiation. *Chemosphere* **2019**, *217*, 833–842. [CrossRef]
44. Engelhart, W.; Dreher, W.; Eibl, O.; Schier, V. Deposition of alumina thin film by dual magnetron sputtering: Is it gamma-$Al_2O_3$? *Acta Mater.* **2011**, *59*, 7757–7767. [CrossRef]
45. Sareen, S.; Mutreja, V.; Singh, S.; Pal, B. Highly dispersed Au, Ag and Cu nanoparticles in mesoporous SBA-15 for highly selective catalytic reduction of nitroaromatics. *RSC Adv.* **2015**, *5*, 184–190. [CrossRef]
46. Wang, Y.; Li, J.; Sun, J.Y.; Wang, Y.B.; Zhao, X. Electrospun flexible self-standing Cu-$Al_2O_3$ fibrous membranes as Fenton catalysts for bisphenol A degradation. *J. Mater. Chem. A* **2017**, *5*, 19151–19158. [CrossRef]
47. Lyu, L.; Zhang, L.L.; Hu, C. Enhanced Fenton-like degradation of pharmaceuticals over framework copper species in copper-doped mesoporous silica microspheres. *Chem. Eng. J.* **2015**, *274*, 298–306. [CrossRef]
48. Sheng, Y.Y.; Sun, Y.; Xu, J.; Zhang, J.; Han, Y.F. Fenton-like degradation of rhodamine B over highly durable Cu-embedded alumina: Kinetics and mechanism. *AlChE J.* **2018**, *64*, 538–549. [CrossRef]
49. Merouani, S.; Hamdaoui, O.; Saoudi, F.; Chiha, M. Sonochemical degradation of Rhodamine B in aqueous phase: Effects of additives. *Chem. Eng. J.* **2010**, *158*, 550–557. [CrossRef]
50. Nieto, L.M.; Hodaifa, G.; Rodriguez, S.; Gimenez, J.A.; Ochando, J. Degradation of organic matter in olive-oil mill wastewater through homogeneous Fenton-like reaction. *Chem. Eng. J.* **2011**, *173*, 503–510. [CrossRef]
51. Hodaifa, G.; Ochando-Pulido, J.M.; Rodriguez-Vives, S.; Martinez-Ferez, A. Optimization of continuous reactor at pilot scale for olive-oil mill wastewater treatment by Fenton-like process. *Chem. Eng. J.* **2013**, *220*, 117–124. [CrossRef]

52. Ma, Q.B.; Hofmann, J.P.; Litke, A.; Hensen, E.J.M. $Cu_2O$ photoelectrodes for solar water splitting: Tuning photoelectrochemical performance by controlled faceting. *Sol. Energy Mater. Sol. Cells* **2015**, *141*, 178–186. [CrossRef]
53. Aylmore, M.G.; Muir, D.M. Thermodynamic analysis of gold leaching by ammoniacal thiosulfate using Eh/pH and speciation diagrams. *Miner. Metall. Process* **2001**, *18*, 221–227. [CrossRef]
54. Lodha, S.; Jain, A.; Punjabi, P.B. A novel route for waste water treatment: Photocatalytic degradation of rhodamine B. *Arab. J. Chem.* **2011**, *4*, 383–387. [CrossRef]
55. Matheson, L.J.; Tratnyek, P.G. Reductive Dehalogenation of Chlorinated Methanes by Iron Metal. *Environ. Sci. Technol.* **2002**, *28*, 2045–2053. [CrossRef]
56. Bjorkbacka, A.; Yang, M.; Gasparrini, C.; Leygraf, C.; Jonsson, M. Kinetics and mechanisms of reactions between $H_2O_2$ and copper and copper oxides. *Dalton Trans.* **2015**, *44*, 16045–16051. [CrossRef]
57. Lousada, C.M.; Jonsson, M. Kinetics, Mechanism, and Activation Energy of $H_2O_2$ Decomposition on the Surface of $ZrO_2$. *J. Phys. Chem. C* **2010**, *114*, 11202–11208. [CrossRef]
58. Lousada, C.M.; Yang, M.; Nilsson, K.; Jonsson, M. Catalytic decomposition of hydrogen peroxide on transition metal and lanthanide oxides. *J. Mol. Catal. A Chem.* **2013**, *379*, 178–184. [CrossRef]
59. Kanel, S.R.; Greneche, J.M.; Choi, H. Arsenic(V) removal kom groundwater using nano scale zero-valent iron as a colloidal reactive barrier material. *Environ. Sci. Technol.* **2006**, *40*, 2045–2050. [CrossRef]
60. Cope, D.B.; Benson, C.H. Grey-Iron Foundry Slags As Reactive Media for Removing Trichloroethylene from Groundwater. *Environ. Sci. Technol.* **2009**, *43*, 169–175. [CrossRef]
61. Agrawal, A.; Tratnyek, P.G. Reduction of Nitro Aromatic Compounds by Zero-Valent Iron Metal. *Environ. Sci. Technol.* **1995**, *30*, 153–160. [CrossRef]
62. Sun, Y.K.; Li, J.X.; Huang, T.L.; Guan, X.H. The influences of iron characteristics, operating conditions and solution chemistry on contaminants removal by zero-valent iron: A review. *Water Res.* **2016**, *100*, 277–295. [CrossRef]
63. Li, H.; Liao, J.Y.; Zeng, T. A facile synthesis of CuO nanowires and nanorods, and their catalytic activity in the oxidative degradation of Rhodamine B with hydrogen peroxide. *Catal. Commun.* **2014**, *46*, 169–173. [CrossRef]
64. Zaman, S.; Zainelabdin, A.; Amin, G.; Nur, O.; Willander, M. Efficient catalytic effect of CuO nanostructures on the degradation of organic dyes. *J. Phys. Chem. Solids* **2012**, *73*, 1320–1325. [CrossRef]
65. Dragoi, M.; Samide, A.; Moanta, A. Discoloration of Waters Containing Azo Dye Congo Red by Fenton Oxidation Process Estimation of activation parameters. *Rev. Chim.* **2011**, *62*, 1195–1198.
66. Martin, R.; Navalon, S.; Delgado, J.J.; Calvino, J.J.; Alvaro, M.; Garcia, H. Influence of the Preparation Procedure on the Catalytic Activity of Gold Supported on Diamond Nanoparticles for Phenol Peroxidation. *Chem. Eur. J.* **2011**, *17*, 9494–9502. [CrossRef]
67. Yao, Z.P.; Chen, C.J.; Wang, J.K.; Xia, Q.X.; Li, C.X.; Jiang, Z.H. Iron Oxide Coating Fenton-like Catalysts: Preparation and Degradation of Phenol. *Chin. J. Inorg. Chem.* **2017**, *33*, 1797–1804.
68. Yang, M.; Zhang, X.; Grosjean, A.; Soroka, I.L.; Jonsson, M. Kinetics and Mechanism of the Reaction between $H_2O_2$ and Tungsten Powder in Water. *J. Phys. Chem. C* **2015**, *119*, 22560–22569. [CrossRef]
69. Ma, J.Q.; Yang, Q.F.; Wen, Y.Z.; Liu, W.P. Fe-g-$C_3N_4$/graphitized mesoporous carbon composite as an effective Fenton-like catalyst in a wide pH range. *Appl. Catal. B* **2017**, *201*, 232–240. [CrossRef]
70. Zhu, J.N.; Zhu, X.Q.; Cheng, F.F.; Li, P.; Wang, F.; Xiao, Y.W.; Xiong, W.W. Preparing copper doped carbon nitride from melamine templated crystalline copper chloride for Fenton-like catalysis. *Appl. Catal. B* **2019**, *256*, 117830. [CrossRef]
71. Ma, J.Q.; Jia, N.Z.F.; Shen, C.S.; Liu, W.P.; Wen, Y.Z. Stable cuprous active sites in Cu+-graphitic carbon nitride: Structure analysis and performance in Fenton-like reactions. *J. Hazard. Mater.* **2019**, *378*, 120782. [CrossRef]
72. Fan, J.W.; Jiang, X.; Min, H.Y.; Li, D.D.; Ran, X.Q.; Zou, L.Y.; Sun, Y.; Li, W.; Yang, J.P.; Teng, W.; et al. Facile preparation of Cu-Mn/$CeO_2$/SBA-15 catalysts using ceria as an auxiliary for advanced oxidation processes. *J. Mater. Chem. A* **2014**, *2*, 10654–10661. [CrossRef]
73. Sun, Y.; Tian, P.F.; Ding, D.D.; Yang, Z.X.; Wang, W.Z.; Xin, H.; Xu, J.; Han, Y.F. Revealing the active species of Cu-based catalysts for heterogeneous Fenton reaction. *Appl. Catal. B* **2019**, *258*, 117985. [CrossRef]
74. Zhang, H.; Zhao, L.X.; Geng, F.L.; Guo, L.H.; Wan, B.; Yang, Y. Carbon dots decorated graphitic carbon nitride as an efficient metal-free photocatalyst for phenol degradation. *Appl. Catal. B* **2016**, *180*, 656–662. [CrossRef]

75. Yu, D.Y.; Li, L.B.; Wu, M.; Crittenden, J.C. Enhanced photocatalytic ozonation of organic pollutants using an iron-based metal-organic framework. *Appl. Catal. B* **2019**, *251*, 66–75. [CrossRef]
76. He, Z.; Sun, C.; Yang, S.G.; Ding, Y.C.; He, H.; Wang, Z.L. Photocatalytic degradation of rhodamine B by $Bi_2WO_6$ with electron accepting agent under microwave irradiation: Mechanism and pathway. *J. Hazard. Mater.* **2009**, *162*, 1477–1486. [CrossRef]
77. Yu, K.; Yang, S.G.; He, H.; Sun, C.; Gu, C.G.; Ju, Y.M. Visible Light-Driven Photocatalytic Degradation of Rhodamine B over $NaBiO_3$: Pathways and Mechanism. *J. Phys. Chem. A* **2009**, *113*, 10024–10032. [CrossRef]
78. Martinez-de la Cruz, A.; Perez, U.M.G. Photocatalytic properties of $BiVO_4$ prepared by the co-precipitation method: Degradation of rhodamine B and possible reaction mechanisms under visible irradiation. *Mater. Res. Bull.* **2010**, *45*, 135–141. [CrossRef]
79. Guo, J.X.; Zhou, H.R.; Ting, S.; Luo, H.D.; Liang, J.; Yuan, S.D. Investigation of catalytic activity and mechanism for RhB degradation by $LaMnO_3$ perovskites prepared via the citric acid method. *New J. Chem.* **2019**, *43*, 18146–18157. [CrossRef]
80. Sun, M.; Li, D.Z.; Chen, Y.B.; Chen, W.; Li, W.J.; He, Y.H.; Fu, X.Z. Synthesis and Photocatalytic Activity of Calcium Antimony Oxide Hydroxide for the Degradation of Dyes in Water. *J. Phys. Chem. C* **2009**, *113*, 13825–13831. [CrossRef]
81. Sharma, G.; Dionysiou, D.D.; Sharma, S.; Kumar, A.; Al-Muhtaseb, A.H.; Naushad, M.; Stadler, F.J. Highly efficient Sr/Ce/activated carbon bimetallic nanocomposite for photoinduced degradation of rhodamine B. *Catal. Today* **2019**, *335*, 437–451. [CrossRef]
82. Natarajan, T.S.; Thomas, M.; Natarajan, K.; Bajaj, H.C.; Tayade, R.J. Study on UV-LED/$TiO_2$ process for degradation of Rhodamine B dye. *Chem. Eng. J.* **2011**, *169*, 126–134. [CrossRef]
83. Khandekar, D.C.; Bhattacharyya, A.R.; Bandyopadhyaya, R. Role of impregnated nano-photocatalyst (SnxTi(1-x)$O_2$) inside mesoporous silica (SBA-15) for degradation of organic pollutant (Rhodamine B) under UV light. *J. Environ. Chem. Eng.* **2019**, *7*, 103433. [CrossRef]
84. Wu, J.; Zhu, K.; Xu, H.; Yan, W. Electrochemical oxidation of rhodamine B by $PbO_2$/Sb-$SnO_2$/$TiO_2$ nanotube arrays electrode. *Chin. J. Catal.* **2019**, *40*, 917–927. [CrossRef]
85. Liu, Y.; Guo, H.G.; Zhang, Y.L.; Cheng, X.; Zhou, P.; Zhang, G.C.; Wang, J.Q.; Tang, P.; Ke, T.L.; Li, W. Heterogeneous activation of persulfate for Rhodamine B degradation with 3D flower sphere-like BiOI/$Fe_3O_4$ microspheres under visible light irradiation. *Sep. Purif. Technol.* **2018**, *192*, 88–98. [CrossRef]